European Journal of
Mineralogy
Open Access

OH incorporation and retention in eclogite-facies garnets from the Zermatt–Saas area (Switzerland) and their contribution to the deep water cycle

Julien Reynes[1,2], Jörg Hermann[2], Pierre Lanari[2], and Thomas Bovay[1,2]

[1]Institute of Earth Sciences, University of Lausanne, Géopolis building,
UNIL-Mouline, 1015 Lausanne, Switzerland
[2]Institute of Geological Sciences, University of Bern, Baltzerstrasse 3, 3012 Bern, Switzerland

Correspondence: Julien Reynes (julien.reynes@unil.ch)

Abstract. The incorporation mechanisms of OH groups in garnet were investigated in a suite of high-pressure rocks from the Zermatt–Saas area (Switzerland) using a combination of Fourier transform infrared spectroscopy (FTIR) and electron probe micro-analysis (EPMA). Investigated garnet specimens include grossular–andradite–uvarovite solid solutions in serpentinite and rodingite and almandine–grossular–pyrope–spessartine solid solutions in eclogite, mafic fels and meta-sediment. All rocks experienced the same peak metamorphic conditions corresponding to a burial depth of $\sim 80\,\mathrm{km}$ ($\sim 540\,^\circ\mathrm{C}$, 2.3 GPa), allowing determination of the OH content in garnet as a function of rock type. The capacity for OH incorporation into garnet strongly depends on its composition. Andradite-rich (400–5000 $\mu\mathrm{g\,g^{-1}}$ H_2O) and grossular-rich garnet (200–1800 $\mu\mathrm{g\,g^{-1}}$ H_2O) contain at least 1 order of magnitude more H_2O than almandine-rich garnet ($< 120\,\mu\mathrm{g\,g^{-1}}$ H_2O). Microscale analyses using FTIR and EPMA profiles and maps reveal the preservation of OH zoning throughout the metamorphic history of the samples. The OH content correlates strongly with Mn, Ca and Ti zoning and produces distinct absorption bands that are characteristic of multiple nano-scale OH environments. The use of 2D diffusion modelling suggests that H diffusion rates in these rocks is as low as $\log(D[\mathrm{m^2\,s^{-1}}]) = -24.5$ at $540\,^\circ\mathrm{C}$. Data were collected for the main garnet-bearing rock types of the Zermatt–Saas area allowing a mass balance model of H_2O to be calculated. The result shows that $\sim 3360\,\mathrm{kg}\,H_2O\,\mathrm{km^{-1}}$ (section of oceanic crust) $\mathrm{yr^{-1}}$ could be transported by garnet in the subducting slab beyond 80 km depth and contributed to the deep-Earth water cycle during the Eocene subduction of the Piemonte–Liguria Ocean.

1 Introduction

The global water budget involves exchanges between three main reservoirs: the atmosphere, the Earth's surface and the Earth's interior. Exchange between the first two reservoirs can be evaluated because they occur on short timescales of days to years (Freeze and Cherry, 1979; Nace, 1971). In contrast, the transfer of water between the surface and the deep Earth occurs on longer timescales (from several Myr to Gyr) and is more challenging to quantify (Rüpke et al., 2004). Today, subduction zones play a critical role in the deep water cycle as the subducted rocks can carry a significant amount of H_2O to mantle depths (Katayama et al., 2006). Water is first stored in hydrous minerals formed during hydrothermal alteration at the ocean floor and is progressively released at depth by metamorphic reactions involving the destabilisation of OH-bearing minerals and the formation of nominally anhydrous minerals (Schmidt and Poli, 1998). Although the main part of the released water escapes the subducting slab and returns to the surface via hydrothermal vents or arc magmatism, the remaining H_2O stored in nominally anhydrous minerals can be carried to greater depth, eventually reaching the mantle transition zone (Peacock, 1990). The estimation of the storage capacity of the subducting oceanic crust is fundamental to quantify the potential effects of subduction on the global water cycle budget of our planet.

Garnet is a key mineral for this purpose as this nominally anhydrous metamorphic mineral forms from depths of ~ 30 km in the subducting oceanic crust (Schmidt and Poli, 1998) and can incorporate water in the form of OH groups where H substitutes for cations in its crystal structure (Cohen-Addad et al., 1967). Garnet displays a wide range of solid solutions and can form in a large variety of rocks. The main endmembers belong to two families: the pyralspite family with almandine (Fe^{2+}/Al^{3+}), pyrope (Mg^{2+}/Al^{3+}) and spessartine (Mn^{2+}/Al^{3+}) endmembers, and the ugrandite family with uvarovite (Ca^{2+}/Cr^{3+}), grossular (Ca^{2+}/Al^{3+}) and andradite (Ca^{2+}/Fe^{3+}). It has been previously demonstrated that endmembers of the ugrandite family have an enhanced ability to incorporate OH groups, up to several weight percent H_2O (Rossman and Aines, 1991; Amthauer and Rossman, 1998; Armbruster et al., 1998), whereas the pyralspite family, especially pyrope- and almandine-rich garnet, are limited to a couple hundred micrograms per gram of H_2O (Aines and Rossman, 1984; Bell et al., 1995; Maldener et al., 2003).

The main point defect enabling H to be incorporated in the garnet structure is the silicon vacancy or hydrogarnet substitution with Si^{4+} replaced by $4H^+$ (Cohen-Addad et al., 1967; Foreman, 1968; Lager et al., 1987). However, the large variety of infrared OH bands observed for such garnets (up to 10 for a single spectrum; e.g. Aines and Rossman, 1984; Rossman and Aines, 1991) and the different behaviour of the OH bands regarding hydrogen diffusion processes (Blanchard and Ingrin, 2004b; Kurka, 2005; Kurka et al., 2005; Reynes et al., 2018) indicate that multiple configurations are present. Several point defects were proposed, such as H^+ taking place in other sites (octahedral–dodecahedral) (Andrut et al., 2002; Basso et al., 1984; Geiger et al., 1991), coupled substitutions such as H–B and H–Li (Lu and Keppler, 1997), or incomplete silicon vacancy coupled with Fe^{2+}/Fe^{3+} or Ti^{4+} (Khomenko et al., 1994; Kühberger et al., 1989; Reynes et al., 2020). A second emerging theory is the interpretation of different infrared OH bands as different degrees of interconnection between hydrogarnet substitutions (Geiger and Rossman, 2020a, b). High-wavenumber bands are allocated to OH groups situated in clustered hydrogarnet substitutions, whereas low-wavenumber bands are interpreted as isolated hydrogarnet substitutions. An alternative interpretation is that the high-wavenumber bands are related to coupled F–H exchanges (Mosenfelder et al., 2022). Identifying different OH defects is essential for the determination of the H retentivity over long timescales.

Previous studies in various locations have shown that high-pressure garnet formed in subduction zones can incorporate significant amounts of OH. Eclogitic garnets from the Kockchetav massif display 10–50 µg g^{-1} H_2O for quartz-bearing eclogites, 80–120 µg g^{-1} H_2O for coesite-bearing eclogites and 130–150 µg g^{-1} H_2O for diamond-grade eclogite (Katayama et al., 2006). Much higher H_2O contents of 14–1900 µg g^{-1} H_2O are reported in eclogitic garnet spec-

imens from Dabie-Sulu (Chen et al., 2007; Sheng et al., 2007; Xia et al., 2005). Ultra-high-pressure (UHP) rocks from the Erzgebirge show 43–84 µg g^{-1} H_2O in eclogitic garnet and 121–241 µg g^{-1} H_2O in garnetite (metarodingite) (Schmädicke and Gose, 2017, 2020; Gose and Schmädicke, 2018). The most H_2O-depleted high-pressure garnet specimens were also reported by these authors from the Lepontine Alps (Cima di Gagnone, CG, and Alpe Arami, AA), with 4–11 µg g^{-1} H_2O in eclogite (AA) and 23–46 µg g^{-1} H_2O in garnetite (CG). In absence of transects from core to rim or H_2O distribution maps, it is challenging to establish whether these H_2O contents reflect the amount of water incorporated during garnet crystallisation under high-pressure conditions or whether they were modified by diffusion during cooling and exhumation.

This study focuses on the quantification of H_2O in garnet and its spatial distribution at the atomic scale (IR-band positions, relationship with chemistry, potential point defects) to the microscale (garnet zoning at the grain scale, correlation with growth stages) and even to the kilometre scale (garnet OH budget in garnet of the subducted oceanic crust). A total of 15 different garnet samples covering the most prominent solid solutions from a full suite of high-pressure rocks were studied by Fourier transform infrared spectroscopy (FTIR) for H_2O determination and electron probe micro-analysis (EPMA) for chemical composition (using transects and maps). The samples come from a subducted portion of oceanic crust and the associated Theodul Glacier Unit (TGU) that are part of the Zermatt–Saas zone (ZS) located in the Western Alps (Switzerland). The large diversity of rock types and garnet compositions makes this area an excellent locality to investigate the H incorporation mechanisms in garnet as well as the H_2O budget in subducted oceanic crust. A major aspect to consider when dealing with high-pressure rocks present at the Earth's surface is whether the features observed were acquired during the burial stage (high pressure) or were partially or completely reset during later exhumation. This leads to the three main questions that are addressed in this paper. (1) How much water can be stored by garnet in deeply subducted oceanic crust? (2) What types of OH defects are present in the different garnet types? (3) Are the original OH contents affected by diffusion after garnet growth?

2   Geological setting and samples

Samples were collected in the ZS and TGU tectonic units during fieldwork in the Zermatt–Saas area or were obtained from the collection of samples from Zermatt of the Natural History Museum of Bern (Naturhistorisches Museum Bern).

The Zermatt–Saas zone is a fragment of the oceanic lithosphere that was part of the Piemonte–Liguria Ocean (Bearth, 1967) formed in the Jurassic, approximatively 164 Myr ago (Allalin gabbro; Rubatto et al., 1998). This fragment was

subducted below the Apulian margin around 40–50 Myr ago (Bowtell et al., 1994; Rubatto et al., 1998) and reached eclogite-facies conditions at a depth of around 80 km. Peak conditions are estimated to be at least 540 °C and 2.3 GPa (550–600 °C, 2.5–3.0 GPa; Bucher et al., 2005; 540 ± 20 °C and 2.3 ± 0.1 GPa; Angiboust et al., 2009), though some studies of the Zermatt–Saas zone give higher conditions (600 ± 20 °C and 2.5 ± 0.3 GPa; Rebay et al., 2018; 600–670 °C and 2.8–3.5 GPa; Luoni et al., 2018). It was eventually rapidly exhumed in the period of 40–35 Ma (Agard et al., 2002; Amato et al., 1999). The area is composed of a diversity of rocks types: serpentinites and associated rodingites (Li et al., 2004); metagabbros (Chinner and Dixon, 1973); metabasalts and hydrothermally altered mafic rocks (Martin et al., 2008); and locally Jurassic to early Cretaceous mafic, pelitic, carbonate-rich and Mn-rich metasediments (Lemoine et al., 1986; Reinecke, 1991). The Theodul Glacier Unit is juxtaposed to the Zermatt–Saas zone and shares a comparable Alpine metamorphic and deformation history. This tectonic unit is composed of complex interlayering between mafic and felsic rocks interpreted as a volcanoclastic to sedimentary sequence that potentially also has relics of Permian metamorphism (Bucher et al., 2019). However, most of the investigated samples come from rock types that were extensively hydrated prior to subduction and show garnet zoning indicative of prograde dehydration reactions (Bovay et al., 2022). The metamorphic peak P (pressure) reached eclogitic conditions (2.65 ± 0.10 GPa and 580 ± 15 °C) and was dated at ∼ 50 Ma (Bovay et al., 2022). During exhumation the tectonic unit was exposed to fluid–rock interaction and subsequent reheating of ∼ 30 °C, starting at 555 ± 15 °C, at a pressure of 1.50 ± 0.10 GPa (Bovay et al., 2021, 2022).

The list of samples, pictures and sample localities are presented in Fig. 1 and Table 1. The samples are described in the following based on the position of their protoliths within the crust.

The first set of samples comes from ultramafic rocks and associated dykes and comprises garnets from the ugrandite family. Sample B2090 is a dark brown to black garnet in a chlorite matrix. Two emerald green samples are identified as Cr-rich andradite (A4544 and 35046); the ZTUv sample occurs in metasomatised mafic dyke in serpentinite (Kempf et al., 2020). The garnet specimens are up to 3 mm in diameter, and green Cr-rich andradite surrounds Cr-rich spinel relics. The rest of the vein is mainly composed of chlorite and microcrystalline brown andradite. Light green to yellow garnet B7415 is characteristic of demantoid (a variety of nearly pure andradite) found in association with asbestos. Sample ZTAdr is a vein containing brown single garnet grains visible at the surface of a serpentinite block from an exposed vein. Grossular-rich garnet was also found among serpentinites and is likely related to mafic dykes that have undergone massive fluid–rock interactions at the oceanic stage (rodingites). Samples B7419 is a dark orange, well-crystallised grossular–andradite. Sample ZTRod is a rodingite consisting of a 60 cm

Table 1. Sample list, rock types, localities and mineral assemblages.

Group	Name	Rock type	Locality/tectonometamorphic unit	GPS location	Assemblage (host rock)	Grt composition	Grt grain size (mm)
G1	Z17TB04B	Mafic fels	Theodul Glacier Unit (TGU)	45°58'17.5'' N, 7°42'38.244'' E	Grt–Diop–Amp–Qtz–Calc	Alm$_{50-59}$Grs$_{32-43}$Pyr$_7$	1–3
G1	Z17TB07	Mafic fels	TGU	45°58'17.5'' N, 7°42'38.244'' E	Grt–Diop–Amp–Zo	Alm$_{40-51}$Grs$_{39-40}$Sps$_{1-15}$	1–4
G1	Z10A	Mafic schist	TGU	45°58'12.5'' N, 7°42'37.544'' E	Grt–white mica–Zo–Qtz	Alm$_{59-65}$Grs$_{25-27}$Pyr$_{6-14}$	0.5–3
G1	Z18TB15	Mafic fels	TGU	45°58'20.9'' N, 7°42'34.8'' E	Grt–Omp–Amp	Alm$_{51-53}$Grs$_{27-34}$Pyr$_{4-14}$	0.5–2
G1	Z17TB03A	Grt-schist	TGU	45°58'18.652' N, 7°42'35.682'' E	Grt–Qtz–white mica–Zo	Alm$_{62-68}$Grs$_{17-27}$Pyr$_{7-13}$	15–30
G1	ZTSps	Garnetite	Trockenersteg/Zermatt–Saas Zone (ZS)	45°58'21'' N, 7°43'12'' E	Grt–phengite–Qtz	Sps$_{48-55}$Alm$_{18-22}$Grs$_{12-13}$	0.015–0.060
G2	ZTRod	Meta-rodingite	Wängie-Unterer / ZS	45°57'56.5914'' N, 7°44'5.928'' E	Grt–Diop–Chl	Grs$_{74-81}$Adr$_{16-24}$	1–10
G2	B7419	Meta-rodingite	Täschtal bei Zermatt / ZS		Grt	Grs$_{68}$Adr$_{23}$	1–10
G2	ZTCarb	Calc-silicate	Trockenersteg / ZS	45°58'23'' N, 7°43'12'' E	Grt–Calc	Grs$_{80}$Adr$_{10}$	0.5–10
G3	35046	Loose sample	Riffelhorn / ZS	Nat. Hist. Museum of Bern	Grt	Grs$_{41}$Uv$_{31}$Adr$_{26}$	?*
G3	B7415	Loose sample	Rimpfischwang / ZS	Nat. Hist. Museum of Bern	Grt + Asbestos	Adr$_{95}$Grs$_5$	1–3
G3	A4544	Loose sample	Riffelhorn, Zermatt / ZS	Nat. Hist. Museum of Bern	Grt	Adr$_{75}$Uv$_{22}$Grs$_3$	?
G3	ZTUv	Grt in mafic dyke	Wängie-Unterer / ZS	45°57'56.5914'' N, 7°44'5.928'' E	Grt (± Uv-rich)	Adr$_{63-79}$Uv$_{5-26}$Grs$_{6-8}$	0.5–2
G3	ZTAdr	Grt vein in ultramafics	Wängie-Unterer / ZS	45°57'51.568''N, 7°43'53.148° E	Grt	Adr$_{63}$Grs$_{30}$CaTiGrt$_6$	2–3
G3	B2090	Chlorite schist	Zermatt end moraine Gornergletscher / ZS	Nat. Hist. Museum of Bern	Grt–Chl	Adr$_{62}$Grs$_{23}$CaTiGrt$_{13}$	0.1–20

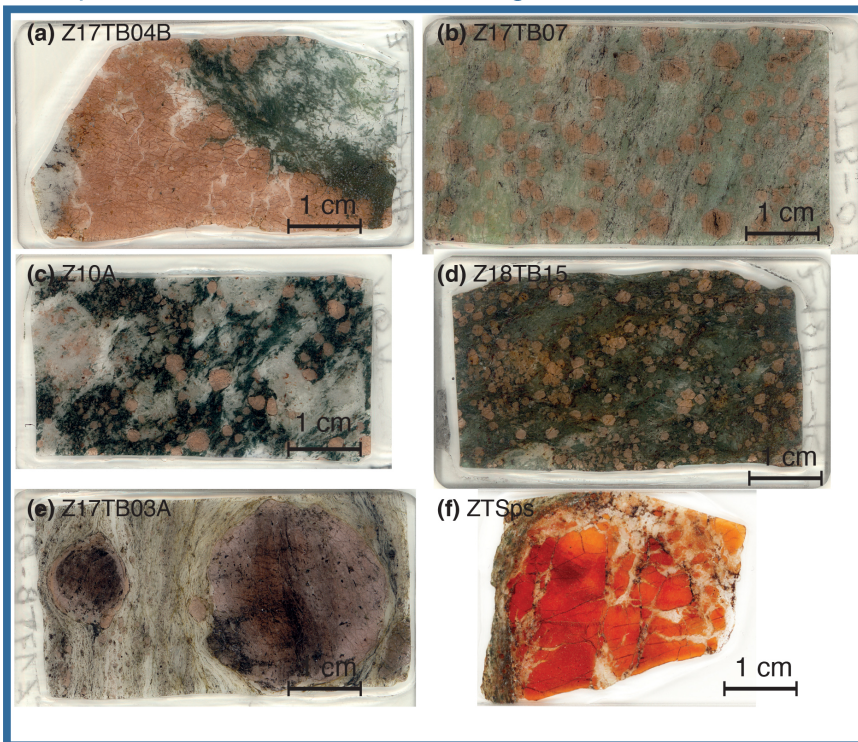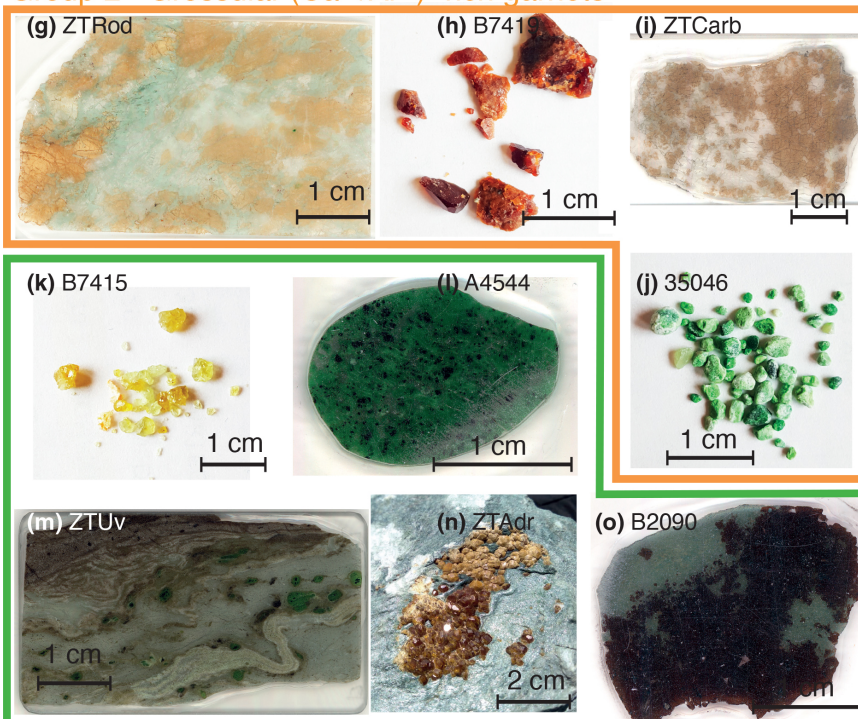* The ? means that the specimen is a microcrystalline aggregate, and the grain size is hard to estimate.

Figure 1. Optical image of analysed samples. **(a–f)** Group 1 samples: **(a–e)** almandine–grossular-rich garnets and **(f)** almandine–spessartine-rich garnet. **(g–i)** Group 2 samples: grossular-rich granite. **(k–o)** Group 3 samples: andradite-rich granite. All pictures were acquired using either an optical scanner (for thick sections) or a camera (for single grains).

large mafic boudin in the ultramafic rocks (Kempf et al., 2020). The rock is composed of diopside and grossular in subequal proportions with minor chlorite.

The mafic rocks were sampled from the Theodul Glacier Unit (Bovay et al., 2022). Sample Z18TB15 is a mafic fels part of a 10 m thick eclogitic body. The mineral assemblage is garnet–omphacite–amphibole. Sample Z17TB04B was taken from an undeformed crosscutting vein in a mafic boudin. The mineral assemblage consists of diopside and garnet with minor amounts of amphibole, quartz and calcite. The vein edge is lined with euhedral garnets. Sample Z17TB07 is a mafic fels that is part of a metre-sized mafic boudin located within a metasedimentary layer and consists of garnet–diopside–amphibole–zoisite formed from a metasomatised Ca-enriched and Na-depleted mafic rock.

The sedimentary cover presents a variety of rock types. Sample Z10A is a foliated mafic schist. The mineral assemblage is garnet (Grt)–white mica–quartz–zoisite, with occurrences of diamond-shaped pseudomorphs after lawsonite consisting of white mica, zoisite and quartz. Sample Z17TB03A is a Grt-schist, where the mineral assemblage quartz-white mica–zoisite defines the main foliation. Large, centimetre-sized garnet porphyroblasts are euhedral with a core rich in inclusions (quartz, zoisite, pyrite and graphite) and a distinct rim. This sample has potentially recorded a polymetamorphic history with a core formed during LP–HT (low-pressure, high-temperature) Permian metamorphism and a rim related to HP–LT (high-pressure, low-temperature) Alpine metamorphism (Bucher et al., 2019). Sample ZTCarb is a metacarbonate composed mainly of calcite and garnet. Finally, sample ZTSps is a nearly pure garnetite of 10 cm diameter that was identified as a metasedimentary former Mn nodule. The grain size is very small, in the range of 15–60 µm. Some zones are optically darker than others. Minor quartz and phengite occur interstitially.

3 Analytical methods

3.1 Electron probe micro analysis (EPMA)

The major-element composition of garnet was determined using a JEOL JXA 8200 superprobe at the Institute of Geological Sciences, University of Bern. Thick sections and epoxy mounts were polished down to $1/4$ µm with diamond paste and carbon coated. The accelerating voltage was set to 15 kV and the beam current to 20 nA for conventional spot analyses. A set of X-ray maps was also acquired using the same accelerating voltage of 15 kV and a beam current of 100 nA. The following elements were measured – Si, Ti, Al, Cr, V, Fe, Mn, Mg and Ca – and calibrated using a set of natural and synthetic standards. Na was not considered because it was < 0.05 wt % near or below the limit of detection. Peak and background were measured for 20 and 2×10 s, respectively, for spot analyses, and a dwell time

of 150 ms was used for mapping. The maps were calibrated and further analysed using XMapTools 3.2.1 (Lanari et al., 2014, 2019). No time-related intensity drift was observed using the monitoring tools available in XMapTools (see discussion and examples in Lanari et al., 2019). The normalisation was realised using an in-house MATLAB® program for 8 cations and 24 charges. The ratio Fe^{2+} / Fe^{3+} was computed based on charge compensation. The amount of H_2O measured by infrared spectroscopy was taken into account in the normalisation, with H taking place as an H_4^{4+} cation in the garnet structural formula. The endmember proportions were calculated based on the octahedral occupancy and secondly corrected by dodecahedral occupancy. CaTiGrt represents a simplified endmember corresponding to the substitution $Al^{3+}Si^{4+} \leftrightarrow Ti^{4+}(Fe^{3+}, Al^{3+})$.

3.2 Fourier transform infrared spectroscopy (MCT-FPA detectors)

FTIR measurements were acquired at the University of Bern using a Bruker FTIR coupled with a HYPERION microscope, equipped with a Plexiglas chamber with controlled airflow and moisture control to limit environmental variations in CO_2 and H_2O (relative humidity < 10 %). This chamber is a key tool to achieve a high signal to noise ratio, which leads to optimal limits of detection. The instrument has two detectors, a single-spot nitrogen-cooled mercury telluride (MCT) detector and a focal plan array (FPA) detector – composed of $64 \times 64 = 4096$ MCT detectors covering a measurement grid of 172.8 µm side length and enabling a minimum pixel size of 2.8 µm. For more details about the method used for FPA mapping, see Reynes et al. (2020). This mapping detector has a lower signal to noise ratio due to the size of the MCT elements leading to higher limits of detection. It is therefore only appropriate for high water contents (over 200 µg g^{-1} H_2O for a 250 µm thick section). For mapping of garnet with low water content (< 100 µg g^{-1} H_2O) it was preferred to use the MCT single-spot detector with a 25–50 µm aperture and a low number of scans to map efficiently the grain.

Measurements were realised on all garnets with a 15× objective and a 4 cm^{-1} (8 cm^{-1} for low-OH, almandine-rich garnet) spectral resolution by transmission infrared spectroscopy. In the case of complete absorbance due to high water contents (over 1500 µg g^{-1} H_2O), the sample was either thinned down or measured with the attenuated total reflectance (ATR) objective. This objective is composed of a germanium crystal tip that is in contact with the sample, enabling measurement of a small interaction volume near the surface (penetration depth < 1 µm) and high water contents (up to wt %). To improve signal quality, it is necessary to measure spectra with 8 cm^{-1} resolution. A concave rubberband baseline correction (OPUS®) was applied to the spectra with 64 points and 4 iterations. Integration method B from OPUS® was used in the OH absorption of garnet (3400–

$3700\,\text{cm}^{-1}$) with boundaries specific for each garnet. The total absorbance is obtained by dividing the integrated area by the sample thickness to obtain the absorption per centimetre. The OH content is then obtained by multiplying the total absorbance by the absorption coefficient k_{abs}. For each sample, k_{abs} is computed using the following relationship:

$$k_{\text{abs}} = \frac{c \times M_{\text{H}_2\text{O}}}{d \times \varepsilon}, \tag{1}$$

where $c = 1 \times 10^6$ is the constant of conversion from grams per gram to micrograms per gram of H_2O, $M_{\text{H}_2\text{O}}$ is the molar mass of H_2O, d is the density of the garnet (in $\text{g}\,\text{L}^{-1}$; computed from EPMA analysis), and ε is the integral molar extinction coefficient (calibration coefficient) determined by an independent method and mineral specific. The coefficient from Maldener et al. (2003) for grossular, $\varepsilon = 14\,400\,\text{L}\,\text{mol}^{-1}\,\text{cm}^{-2}$, was chosen for grossular- and andradite-rich garnet specimens, as previous studies have shown it to be appropriate for these garnet compositions (Reynes et al., 2018, 2020). In the case of almandine-rich garnet specimens, including the spessartine–almandine solid-solution ZTSps, the coefficient of Bell et al. (1995) for pyrope–almandine garnet, $\varepsilon = 6700\,\text{L}\,\text{mol}^{-1}\,\text{cm}^{-2}$, was used as there is no other robust calibration available for almandine-rich garnet. Maldener et al. (2003) provided various coefficients for very similar compositions of almandine-rich garnet ($2370–6340\,\text{L}\,\text{mol}^{-1}\,\text{cm}^{-2}$), calibrated by nuclear reaction analysis on garnet with H_2O contents near the detection limit ($< 50\,\mu\text{g}\,\text{g}^{-1}\,H_2O$). The coefficient of Bell et al. (1995) presents two advantages. Firstly, compared to the range of coefficients determined by Maldener et al. (2003), it represents a conservative estimate of the water content. Secondly, most of the previous studies that evaluated water in eclogitic garnets did use this coefficient (Katayama et al., 2006; Schmädicke and Gose, 2020; Gose and Schmädicke, 2018; Schmädicke and Gose, 2017), and thus this facilitates the comparison of our results for garnets from the Zermatt–Saas area with other localities.

The thickness of all samples was measured using a Mitutoyo® micrometre with an accuracy of $\pm\,2\,\mu\text{m}$. Additionally, the overtone domain ($1550–2000\,\text{cm}^{-1}$) was integrated for each spectrum as well, which enables in situ thickness determination using

$$\text{Thickness}\,(\mu\text{m}) = r \times \text{Abs}(1550 - 2000\,\text{cm}^{-1}). \tag{2}$$

The constant r is the ratio between the measured thickness of the sample using a mechanical micrometre and the average overtone area of the analysed sample. This advantage is twofold: (1) it corrects the possible edge effect on transects when measuring grains that are slightly thicker in their core than in their rim due to the polishing method, and (2) it excludes spectra that are not characteristic of garnet. The value of r varies from andradite–grossular- ($r = 1.20–1.30$) to almandine-rich garnets ($r = 1.40–1.44$).

3.3 Diffusion modelling

A MATLAB® algorithm was developed to model hydrogen diffusion in garnet over short and long timescales. A 2D diffusion equation in a semi-infinite medium was used (Crank, 1975, p. 150, Eq. 8.46). It assumes the garnet to be infinite in the third dimension; this can cause minor artefacts (diffusion mechanism may be slightly faster than modelled).

$$\frac{\partial C}{\partial t} = D\left(\frac{\partial^2 C}{\partial x^2} + \frac{\partial^2 C}{\partial y^2}\right), \tag{3}$$

where D is the diffusion coefficient (in $\text{m}^2\,\text{s}^{-1}$) and $C(x, y, t)$ the mass fraction of H_2O in garnet (in $\mu\text{g}\,\text{g}^{-1}\,H_2O$). A 2D numerical solution was used to approximate $C(x, y, t)$ by the discrete function $c_{i,j}^n$, where $x = i\Delta x$, $y = j\Delta y$ and $t = n\Delta t$. The finite difference approximation is

$$\frac{c_{i,j}^{n+1} - c_{i,j}^n}{\Delta t} = D\left[\frac{c_{i+1,j}^n - 2c_{i,j}^n + c_{i-1,j}^n}{(\Delta x)^2} \right.$$
$$\left. + \frac{c_{i,j+1}^n - 2c_{i,j}^n + c_{i,j-1}^n}{(\Delta y)^2}\right]. \tag{4}$$

The state of the system at step $n+1$ ($c_{i,j}^{n+1}$) can then be calculated from its state at time step n ($c_{i,j}^n$). The maximum time step Δt that is possible to prevent the solution from becoming unstable is given by

$$\Delta t_{\text{max}} = \frac{1}{2D}\frac{(\Delta x \Delta y)^2}{(\Delta x)^2 + (\Delta y)^2}. \tag{5}$$

The algorithm takes as entry a hypothetical OH content map of the crystal with water zoning, a diffusion coefficient (in $\text{m}^2\,\text{s}^{-1}$) and a total duration time in seconds (s) for the experiment. It returns the computed OH maps at different time steps from initial to the end of the duration of the experiment.

4 Results

4.1 Chemical composition of garnet

Representative chemical compositions of garnet samples are reported in Table 2. For some samples, chemical maps were acquired on selected grains, and characteristic chemical maps are represented in Figs. 2 and 3 (other endmember maps are available in Fig. S1, available online as the Supplement linked to this article on the website of the journal https://ejm.copernicus.org/). Three groups of garnet are described below.

Group 1 (Fig. 1) consists of almandine-rich garnets ($\text{Alm}_{40–68}$) with relatively high grossular ($\text{Grs}_{12–43}$) and variable proportions in other endmembers. Most of them are presenting core to rim chemical zoning, as highlighted by Fig. 2. Sample Z17TB04B is showing a rim enriched in CaO ($15.33\,\text{wt}\,\%$) compared to its core ($11.51\,\text{wt}\,\%$),

Table 2. Representative composition of garnet analysed in the study determined by EPMA.

	Z17TB04B Rim (4)	Z17TB04B Core (6)	Z17TB07 Rim (7)	Z17TB07 Mantle (7)	Z17TB07 Core (7)	Z10A Rim (8)	Z10A Core (5)	Z18TB15 Rim (8)	Z18TB15 Core (8)	Z17TB03A Rim (10)	Z17TB03A Mantle (10)	Z17TB03A Core (7)	ZTSps LMnZ	ZTSps HMnZ	ZTRod Type I (4)	ZTRod Type II (3)	B7419 Mean (10)	ZTCarb Mean (5)	35046 Mean (10)	B7415 Mean (10)	A4544 Mean (10)	ZTUv RimZ	ZTUv CoreZ	ZTAdr Mean (8)	B2090 Mean (20)
SiO_2	38.63	38.14	38.30	37.97	37.96	38.49	37.94	37.40	37.07	38.22	38.46	38.50	37.05	37.20	36.88	37.50	37.73	38.50	36.88	35.48	35.54	34.42	34.92	36.02	34.09
TiO_2	0.12	0.10	0.07	0.11	0.13	0.04	0.10	0.04	0.14	0.10	0.02	0.08	0.19	0.16	0.10	0.29	0.84	0.97	0.26	0.00	0.11	2.49	1.53	1.85	4.00
Al_2O_3	21.51	21.44	21.56	21.25	21.20	22.51	22.17	21.30	20.51	21.40	21.50	21.53	20.14	20.19	17.08	18.84	15.75	19.54	8.83	0.86	0.28	1.33	1.30	5.60	4.25
Cr_2O_3	0.02	0.01	0.01	0.01	0.01	0.02	0.02	0.04	0.03	0.01	0.02	0.01	bdl	bdl	0.02	0.10	0.01	0.02	9.61	bdl	6.68	1.44	7.94	bdl	0.08
$FeOt$	22.80	27.01	23.81	21.47	18.85	27.71	29.91	26.18	24.33	30.01	31.43	28.61	12.94	10.21	7.23	4.81	10.12	5.38	8.01	27.16	21.43	22.67	18.13	19.53	19.55
Fe_2O_3	0.01	0.18	0.21	0.54	0.49	0.31	0.13	1.89	0.13	0.01	0.19	1.41	2.91	2.27	8.02	5.35	7.86	3.30	8.69	30.18	23.51	25.19	20.14	20.49	19.87
FeO	22.79	26.85	23.62	20.98	18.41	27.43	29.79	24.48	23.06	30.00	31.26	28.60	10.32	8.17	0.01	0.00	3.05	2.41	0.19	0.00	0.28	0.00	0.01	1.09	1.67
MnO	0.32	0.71	0.44	4.12	6.98	0.18	0.30	0.07	3.24	0.23	0.67	0.55	22.07	25.39	0.95	0.79	0.32	0.30	0.53	0.04	0.05	0.22	0.31	0.23	0.31
MgO	1.73	1.89	1.99	0.77	0.61	3.75	1.54	3.64	0.93	1.77	3.47	2.35	2.26	1.85	0.07	0.18	bdl	0.51	bdl	bdl	bdl	0.55	0.16	bdl	bdl
CaO	15.33	11.51	14.23	14.81	14.79	9.18	9.86	10.71	12.84	9.62	6.15	9.88	6.05	5.85	34.85	34.77	33.45	33.98	34.28	33.51	33.07	33.66	34.01	34.27	33.85
H_2O^*	0.010	0.004	0.004	0.008	0.010	0.001	0.004	0.001	0.005	0.003	0.001	0.002	0.003	0.026	0.039	0.046	0.184	0.131	0.161	0.054	0.047	0.350	0.208	0.249	0.500
Total	100.5	100.8	100.5	100.6	100.6	101.9	101.8	99.56	99.23	101.4	101.7	101.5	101.0	101.1	98.00	97.86	99.20	99.65	99.44	100.1	99.56	99.65	100.5	99.82	98.62
Si	3.017	2.996	2.995	2.990	2.992	2.966	2.967	2.950	2.977	3.004	3.003	3.007	2.955	2.969	2.908	2.932	2.964	2.950	2.974	2.980	3.002	2.880	2.900	2.950	2.844
Ti	0.007	0.006	0.004	0.007	0.008	0.003	0.006	0.002	0.008	0.006	0.001	0.005	0.011	0.010	0.006	0.017	0.050	0.056	0.016	0.000	0.007	0.157	0.096	0.114	0.251
Al	1.980	1.985	1.988	1.972	1.969	2.044	2.044	1.980	1.942	1.983	1.979	1.982	1.893	1.899	1.587	1.737	1.458	1.765	0.839	0.085	0.028	0.131	0.127	0.541	0.417
Cr	0.001	0.001	0.001	0.000	0.001	0.001	0.001	0.003	0.002	0.001	0.001	0.001	0.000	0.000	0.001	0.006	0.001	0.001	0.613	0.000	0.446	0.095	0.521	0.000	0.005
Fe^{3+}	0.001	0.011	0.012	0.032	0.029	0.018	0.008	0.112	0.085	0.001	0.011	0.001	0.175	0.136	0.476	0.315	0.465	0.190	0.527	1.908	1.494	1.586	1.258	1.263	1.248
Fe^{2+}	1.488	1.764	1.545	1.382	1.214	1.767	1.949	1.615	1.549	1.972	2.041	1.868	0.689	0.546	0.001	0.000	0.201	0.154	0.013	0.000	0.020	0.000	0.000	0.075	0.116
Mn	0.021	0.048	0.029	0.275	0.466	0.012	0.020	0.004	0.220	0.015	0.045	0.037	1.491	1.717	0.063	0.052	0.021	0.019	0.036	0.003	0.004	0.016	0.022	0.016	0.022
Mg	0.202	0.222	0.232	0.091	0.072	0.431	0.179	0.428	0.112	0.207	0.404	0.274	0.269	0.220	0.008	0.021	0.000	0.058	0.000	0.000	0.000	0.068	0.020	0.000	0.000
Ca	1.282	0.969	1.193	1.250	1.249	0.758	0.826	0.906	1.105	0.811	0.514	0.827	0.517	0.500	2.944	2.913	2.816	2.790	2.961	3.016	2.993	3.017	3.026	3.007	3.026
H_4	0.001	0.001	0.001	0.001	0.001	0.000	0.001	0.000	0.001	0.000	0.000	0.000	0.000	0.003	0.005	0.006	0.024	0.017	0.022	0.008	0.007	0.049	0.029	0.034	0.070
CaTi-grt	0.00	0.00	0.00	0.00	0.00	0.00	0.00	0.00	0.00	0.00	0.00	0.00	0.01	0.00	0.00	0.01	0.02	0.03	0.01	0.00	0.00	0.08	0.05	0.06	0.13
Adr	0.00	0.01	0.01	0.02	0.01	0.01	0.00	0.06	0.04	0.00	0.01	0.00	0.09	0.07	0.24	0.16	0.23	0.10	0.26	0.954	0.75	0.79	0.63	0.63	0.62
Uv	0.00	0.00	0.00	0.00	0.00	0.00	0.00	0.00	0.00	0.00	0.00	0.00	0.00	0.00	0.00	0.00	0.00	0.00	0.31	0.00	0.22	0.05	0.26	0.00	0.00
Grs	0.43	0.32	0.39	0.40	0.40	0.25	0.27	0.27	0.34	0.27	0.17	0.27	0.12	0.13	0.74	0.81	0.68	0.80	0.41	0.046	0.03	0.08	0.06	0.30	0.23
Sps	0.01	0.02	0.01	0.09	0.15	0.00	0.01	0.00	0.07	0.01	0.01	0.01	0.48	0.55	0.02	0.02	0.01	0.01	0.01	0.00	0.00	0.00	0.00	0.00	0.00
Alm	0.50	0.59	0.51	0.46	0.40	0.59	0.65	0.53	0.51	0.66	0.68	0.62	0.22	0.18	0.00	0.00	0.06	0.05	0.00	0.00	0.00	0.00	0.00	0.01	0.01
Pyr	0.07	0.07	0.08	0.03	0.02	0.14	0.06	0.14	0.04	0.07	0.13	0.09	0.09	0.07	0.00	0.01	0.00	0.02	0.00	0.00	0.00	0.00	0.00	0.00	0.00
Density	3.89	3.96	3.91	3.92	3.92	3.97	3.99	3.94	3.95	3.99	4.02	3.98	4.05	4.06	3.66	3.63	3.69	3.64	3.67	3.88	3.82	3.85	3.79	3.80	3.81
k_{abs}	0.69	0.68	0.69	0.69	0.68	0.68	0.67	0.68	0.68	0.67	0.67	0.68	0.31	0.31	0.34	0.34	0.34	0.34	0.34	0.32	0.33	0.32	0.33	0.33	0.33
Cal.	B	B	B	B	B	B	B	B	B	B	B	B	M	M	M	M	M	M	M	M	M	M	M	M	M

* Measured by FTIR; RimZ is rim zone, CoreZ is core zone, LMnZ is low-Mn zone and HMnZ is high-Mn zone. For these samples, an average composition was determined using the average composition of n pixels within an area and reported as mean (n). bdl signifies below detection limit, and CaTi-grt corresponds to a simplified endmember $Ca_3Ti_2(Fe,Al)_2SiO_{12}$. k_{abs} is the absorption coefficient (in cm^2), and Cal. is the calibration coefficient chosen. $B = 6700\,L\,mol^{-1}\,cm^{-1}\,cm^{-2}$ from Bell et al. (1995); $M = 14400\,L\,mol^{-1}\,cm^{-1}\,cm^{-2}$ from Maldener et al. (2003).
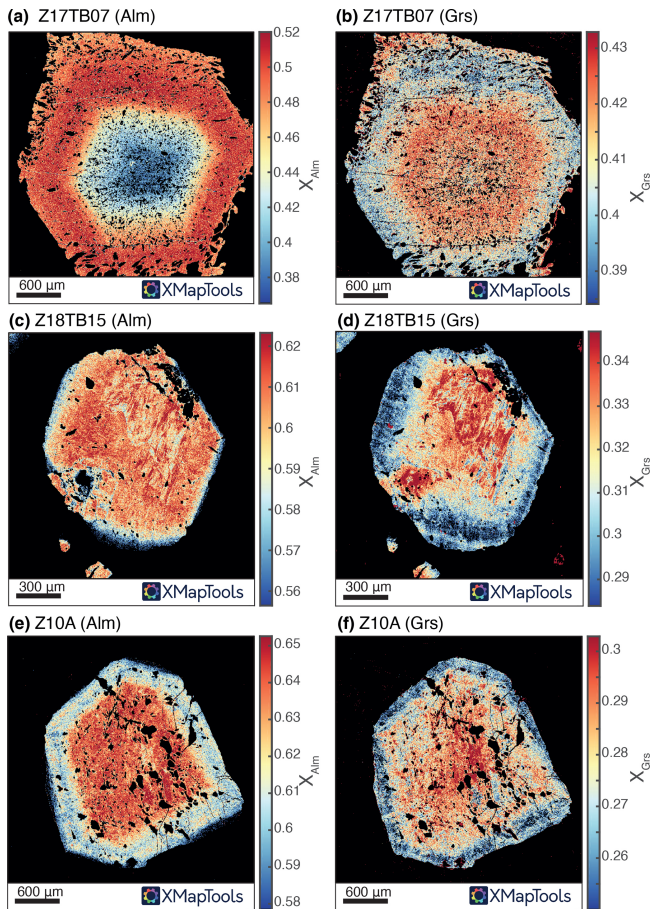
Figure 2. Compositional maps (endmember proportion) of garnet obtained from X-ray maps measured by EPMA and processed using the XMapTools software. **(a)** Map of the proportion of the almandine component (X_{Alm}) of sample Z17TB07. **(b)** Map of the proportion of the grossular component (X_{Grs}) of sample Z17TB07. **(c)** X_{Alm} map of sample Z18TB15. **(d)** X_{Grs} map of sample Z18TB15. **(e)** X_{Alm} map of sample Z10A. **(f)** X_{Grs} map of sample Z10A.

whereas samples Z18TB15 and Z10A are showing an enriched core (12.84 wt % and 9.86 wt %) compared to their rims (10.71 wt % and 9.18 wt %). Sample Z17TB03A shows a core and rim enriched in CaO (respectively 9.88 wt % and 9.62 wt %) compared to its mantle (6.15 wt %). The sample Z17TB07 has a rather constant CaO content (14 wt %–15 wt %). Sample ZTSps ($Sps_{48-55}Alm_{18-22}Grs_{12-13}$) is included in this group, though its chemistry is more spessartine-rich (Fig. 3).

Group 2 (Fig. 1) is identified as grossular (Grs_{41-81}) with minor components of uvarovite (Uv_{0-31}) and andradite (Adr_{10-26}) and very low almandine component (Alm_{0-6}). Sample ZTCarb and B7419 display a minor almandine component (Alm_{5-6}). Sample ZTRod is showing two garnet types (type I and type II). Type I ($Grs_{74}Adr_{24}$) is slightly richer in the andradite component compared to type II ($Grs_{81}And_{16}$). Another difference is in minor TiO_2 con-

tent, as type II contains 3 times more Ti compared to type I (respectively 0.10 wt % and 0.29 wt % TiO_2). Sample 35046 shows the most heterogeneous garnet composition with a subequal amount of uvarovite and andradite $Grs_{41}Uv_{31}Adr_{26}$.

Group 3 (Fig. 1) consists of andradite-rich garnet specimens (Adr_{62-95}) with a significant proportion of substitution of Fe^{3+} by Ti^{4+} and/or Cr^{3+}. Sample B7415 is a nearly pure andradite (Adr_{95}) with a minor grossular component. Samples A4544 and the core of ZTUv have a main andradite component (Adr_{63-75}) and a secondary uvarovite component (Uv_{22-26}). Samples ZTUv rim and ZTAdr are andradite rich (Adr_{63-79}) with ∼ 2 wt % TiO_2. For sample ZTUv, a rim enriched in Ti is clearly identifiable (up to 2.5 wt % TiO_2 versus 1.5 wt % TiO_2 in the core). Sample B2090 is a titanium andradite ($And_{62}Grs_{23}CaTiGrt_{13}$) with the highest TiO_2 content reported among these garnets (4 wt % TiO_2).

4.2   IR spectra and band positions

The FTIR spectra of the OH region of garnet (3400–3700 cm^{-1}) are presented in Fig. 4. The spectra are shown for the groups identified in Fig. 1. The almandine-rich garnets of group 1 show rather low absorption with an OH band intensity of less than 2 for a thickness normalised to 1 cm (with the exception of sample ZTSps). The spectra are dominated by a band centred on 3550 cm^{-1} characteristic of almandine-rich garnet as shown by Aines and Rossman (1984). Almandine-rich garnet from samples Z17TB04B, Z17TB07 and Z10A shows OH bands in the domain 3550–3650 cm^{-1} that are in the same range of intensity as the main band at 3550 cm^{-1}. The low-Mn zone of sample ZTSps shows a single band centred at 3555 cm^{-1} and of similar intensity to the other almandine samples. The high-Mn zone of this sample displays five bands, 3500, 3517, 3560, 3591 and 3640 cm^{-1}, at an intensity level of 4 times that observed for the low-Mn zone. These bands were already identified for spessartine garnet (Reynes et al., 2018). For the core of sample Z17TB07 it was impossible to avoid the numerous tiny inclusions of amphibole, and the spectrum has the form of the triplet 3646–3660–3674 cm^{-1}. In order to estimate the water content of garnet in this sample, in this domain the absorption of the amphibole was subtracted from the measured OH absorption. Phengite is another possible hydrous phase that can occur as inclusion in garnet. Phengite has a strong absorbance band at 3623 cm^{-1}, which was not observed in these spectra. Clinozoisite and chlorite have absorption bands at wavenumbers < 3450 cm^{-1} and are thus easily detected. The spectra do not display any contamination of chlorite and clinozoisite.

The OH absorption bands for Ca-rich garnet (groups 2 and 3) are displayed in Fig. 4b. For these two groups, the absorbance measured is 1 order of magnitude higher than for garnet of group 1. Samples ZTCarb, B7419 and ZTRod type II are showing similar band positions, with a main doublet at 3596–3598 and 3611 cm^{-1}. Secondary broad bands at 3557
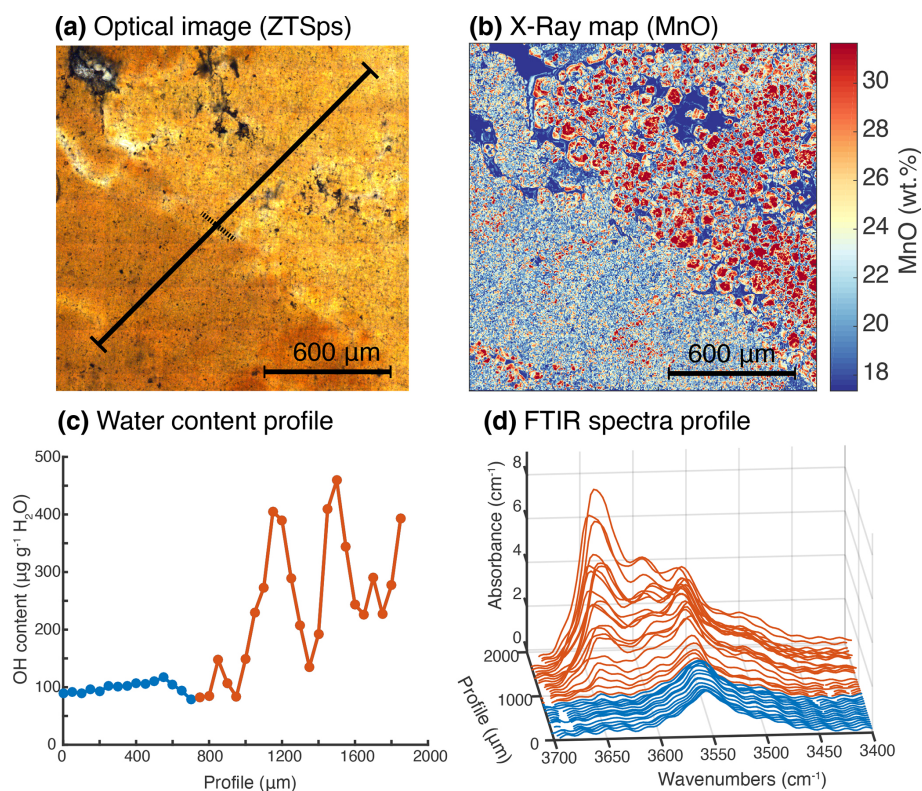
Figure 3. Optical image, compositional map and FTIR transects for sample ZTSps. **(a)** Optical image (transmission) of sample ZTSps highlighting dark and light zones. **(b)** MnO map expressed (in wt %) of the same area presented in **(a)**. **(c)** H_2O concentration profile (expressed as $\mu g\,g^{-1}$ H_2O) acquired with $40\,\mu m$ step and $40\,\mu m$ spot size. The blue part corresponds to the dark, lower-Mn zones presented in **(a)**, the orange part corresponds to the light, higher-Mn zone presented in **(a)**. **(d)** Stacked FTIR spectra measured in the OH stretching region (3400–$3700\,cm^{-1}$) across the profile with the same colour code as in **(c)**.

and $3656\,cm^{-1}$ are clearly identified. The sample B7419 has a more pronounced band at $3583\,cm^{-1}$ that only appears as a shoulder in spectra from ZTCarb and ZTRod type II. The sample ZTRod type I spectrum is characterised by a doublet at 3614–$3621\,cm^{-1}$; the band at $3621\,cm^{-1}$ does not appear on spectra from sample ZTRod type II. Grossular–uvarovite 35046 has an asymmetric main band at $3617\,cm^{-1}$ with a shoulder at around $3600\,cm^{-1}$ and a broad band at $3550\,cm^{-1}$. Andradite garnet shows more complex spectra with up to six different bands. Near-endmember andradite garnet samples B7415 and A4544 show the simplest spectra with only two well-defined bands, the main at $3564\,cm^{-1}$ and a secondary at $3606\,cm^{-1}$. The spectra obtained for the core of sample ZTAdr and for B2090 are very similar, with two main bands at around 3560 and $3600\,cm^{-1}$ and shoulders at 3580 and $3640\,cm^{-1}$. Despite these similarities, the position of the main bands is not identical, with one located at $3557\,cm^{-1}$ for sample B2090 and at $3561\,cm^{-1}$ for ZTAdr. The second main bands are at $3600\,cm^{-1}$ for sample ZTAdr and at $3607\,cm^{-1}$ for sample B2090. Sample ZTUv shows similar band positions for the core and the rim spectra, and only intensities appear to change. The main doublet at 3565–

$3576\,cm^{-1}$ is followed by a well-defined band at $3605\,cm^{-1}$ and some minor shoulders at 3620 and $3640\,cm^{-1}$.

4.3 OH content in garnet and effect of chemical composition

Table 3 reports the total absorbance (integrated area per centimetre) and OH contents calculated for each sample (formally expressed in $\mu g\,g^{-1}$ H_2O). The range of OH contents measured in a sample is indicated with minimum and maximum values. The column "mean" gives the average and the standard deviation of the measured data. For analyses of group 1 the OH content ranges from 2 to $115\,\mu g\,g^{-1}$ H_2O with the exception of the spessartine-rich garnet in sample ZTSps that reaches $550\,\mu g\,g^{-1}$ H_2O (Table 3). Analyses from group 2 show higher OH contents from 180 to $2400\,\mu g\,g^{-1}$ H_2O. Sample ZTRod is showing the lowest range of OH content (172–$524\,\mu g\,g^{-1}$ H_2O), while other samples of this group have over $1000\,\mu g\,g^{-1}$ H_2O. Analyses from group 3 display the highest measured water content, from 400 to $5900\,\mu g\,g^{-1}$ H_2O. Nevertheless, high disparities appear in this group, with samples B7415 and A4544 showing moderate water contents (400–$740\,\mu g\,g^{-1}$ H_2O),
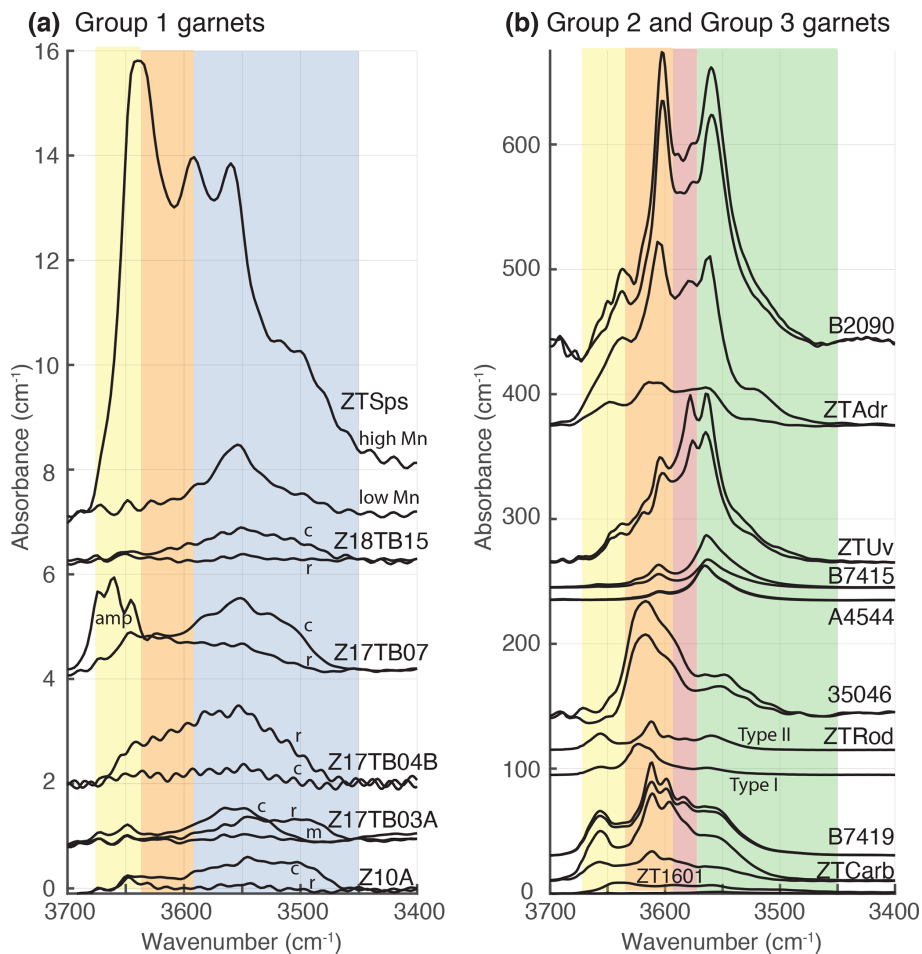
Figure 4. Infrared spectra in the OH stretching domain of garnet (3400–$3700 \, \mathrm{cm}^{-1}$). All intensities are normalised to a thickness of 1 cm. In **(a)**, group 1 samples as defined in Fig. 1 (almandine-rich garnet) and, in **(b)**, the group 2 and 3 samples (Ca-rich garnet) are represented. For all samples, at least two spectra are plotted to show the diversity of spectra acquired in the same grain. Colour stripes correspond to wavenumber domains associated with OH defects for common garnet endmembers: in blue for almandine, orange and yellow for grossular, green for andradite, and red for Ti-rich garnet. More details are given in the text. Band abbreviations: c – core; m – mantle; r – rim; amp – amphibole bands.

whereas samples ZTUv, ZTAdr and B2090 display OH contents over $1000 \, \mathrm{\mu g \, g^{-1}}$ H_2O. The relationship between the garnet major-element composition and the water content determined by FTIR is displayed in Fig. 5. The Ca-rich garnets of groups 2 and 3 are the most enriched in OH ($> 350 \, \mathrm{\mu g \, g^{-1}}$ H_2O; Fig. 5a, c). For group 3, the samples with the highest sum of Ca endmembers are relatively depleted in OH (e.g. samples B7415 and A4544) compared to samples ZTUv and ZTAdr. The analyses of almandine-rich garnet of group 1 show a positive correlation between the OH content and the grossular component (Fig. 5c) – there are neither andradite nor uvarovite components in these garnets. The only exception is the spessartine-rich garnet from sample ZTSps, showing that Mn enhances the capacity to incorporate H_2O. Analyses from groups 2 and 3 show a positive correlation with titanium (Fig. 5b, d). However, most analyses plot above the 1 : 1 ratio between molar Ti and H (black line) indicating that

not all H_2O can be accommodated by a $Ca_3Ti_2H_2Si_2O_{12}$ hydrous endmember (see Reynes et al., 2020). Such a close relationship between TiO_2 content and H_2O is also visible on the maps of sample ZTUv (Fig. 6d, f), with a rim enriched in both TiO_2 and H_2O. Finally, analyses from group 1 display a positive correlation between TiO_2 and H_2O for most samples, but data are more scattered than for groups 2 and 3 (Fig. 5d).

4.4 Hydrogen zoning

Zoning of OH was investigated in all sample groups using transects and maps (Figs. 6, 7). A special focus is placed on garnet from group 1. Figures 6 and 7 display a map and transects of the OH contents in these almandine-rich garnets. Transects were acquired using a clean surface and avoiding fractures and mineral inclusions whenever possible.

Table 3. Fourier transform infrared spectroscopy results and OH content determination.

Name	Range of integration (cm^{-1})	Total absorbance (cm^{-1})			Water content (µg g^{-1} H$_2$O)			OH band position (cm^{-1})
		Min	Max	Mean (SD)	Min	Max	Mean (SD)	
Z17TB04B	[3450–3660]	27	162	98 (48)	18	105	64 (24)	**3553**
Z17TB07	[3450–3625]	50	124	96 (20)	34	86	66 (14)	**3551**
Z10A	[3450–3625]	3	81	34 (23)	2	55	23 (16)	3500–**3546**–3631
Z18TB15	[3450–3650]	3	127	45 (29)	2	86	31 (20)	**3551**
Z17TB03A	[3450–3625]	2.95	39	15 (13)	2	27	10 (9)	**3554**
ZTSps	[3450–3670]	81	840	271 (185)	53	554	179 (122)	3500–**3554**–**3560**–3591–**3640**
ZTRod	[3500–3675]	505	1541	1032 (163)	172	524	351 (55)	3560–3583–3597–**3611**–**3623**–3656
B7419	[3500–3675]	4743	6714	5421 (574)	1613	2283	1843 (195)	3556–3583–**3598**–**3611**–3657
ZTCarb	[3500–3675]	2010	5817	3864 (759)	683	1978	1314 (258)	3556–**3596**–**3611**–3657
35046	[3500–3675]	3154	6940	4730 (1105)	1072	2360	1608 (376)	3546–**3617**
B7415	[3500–3640]	1197	2309	1685 (370)	383	739	539 (118)	**3564**–3606
A4544	[3500–3640]	1343	1566	1416 (70)	443	517	467 (23)	**3566**–3604
ZTUv	[3450–3675]	6302	10 605	7296 (737)	2080	3500	2408 (243)	**3565**–**3578**–3605
ZTAdr	[3450–3675]	3183	15 356	7546 (2206)	1050	5067	2490 (728)	**3561**–3580–**3607**–3637
B2090	[3450–3675]	12 291	18 352	15 620 (1887)	3933	5873	4998 (604)	**3557**–**3600**–3637

SD is standard deviation. The numbers in bold are the main OH band positions.
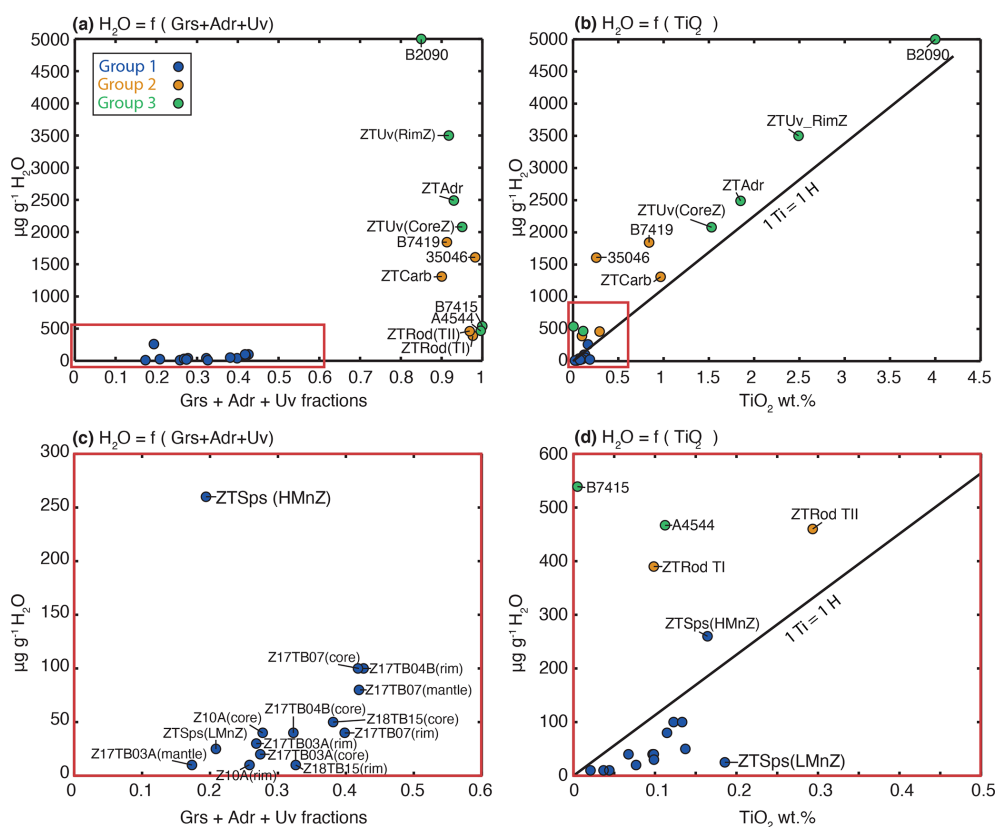
Figure 5. Compositional plots comparing OH contents and Ca–Ti contents in garnet. **(a)** H$_2$O content in garnet (µg g^{-1} H$_2$O) as a function of the sum of the Ca–garnet endmember fractions ($X_{Grs} + X_{Adr} + X_{Uv}$). Colour code follows the garnet groups as identified in Fig. 1. **(b)** OH content in garnet as a function of TiO$_2$ (unit wt %). The black line corresponds to the 1 : 1 molar proportion for H and Ti. Colour code is identical to **(a)**. Panels **(c)** and **(d)** are, respectively, zooms of the red boxes represented on graphs **(a)** and **(b)**.

The values measured for each spot were then projected orthogonally on the profile line. Samples Z18TB15, Z10A and Z17TB07 show a concave behaviour: the core is more enriched in OH than the rim (Fig. 7b, d, f). For all samples a factor of 2 to 3 increase is observed from rim to core. The transect across sample Z18TB15 displays two main zones: a 400 μm wide rim containing 25 μg g^{-1} H$_2$O and a 200 μm core with 50 μg g^{-1} H$_2$O. Garnet Z10A shows two main optical zones in Fig. 7c. The transition from the optically brownish core (Fig. 7c, d) with $\sim$ 40 μg g^{-1} H$_2$O to the rim containing $\sim$ 10 μg g^{-1} H$_2$O is sharp. Garnet Z17TB07 (Fig. 7e, f) shows three distinct OH zones. The 1000 μm wide core is dark (Fig. 7e) due to the high density of amphibole inclusions (note that these are filtered out when computing the OH content). The H$_2$O contents vary from 100 μg g^{-1} H$_2$O in the inner core to 80 μg g^{-1} H$_2$O in the outer core. The 400 μm wide mantle zone shows $\sim$ 80 μg g^{-1} H$_2$O and appears optically brownish (Fig. 7e). The rim, optically lighter than the mantle, shows 50 μg g^{-1} H$_2$O, a value that is half of the inner core content. The sample Z17TB04B shows a rim that is slightly richer in OH than the mantle and core zones. The map of sample Z17TB04B (Fig. 6c) reveals a rim (100 μg g^{-1} H$_2$O) 5 times richer in OH than the core (20 μg g^{-1} H$_2$O). Sample Z17TB03A shows a rim with already low OH contents (30 μg g^{-1} H$_2$O) and a core with very low OH (5–10 μg g^{-1} H$_2$O). The spessartine-rich garnet (sample ZTSps) displays two optical zones (Fig. 3a), a darker and a light zone, which correspond chemically to a Mn-depleted and Mn-enriched zone, respectively (Fig. 3b). Because the grain size is very small (10–20 μm), the FTIR spot provides an average content of a zone of 25 × 25 μm^2. The H$_2$O content is constant at around 100 μg g^{-1} H$_2$O in the dark zone but shows a high degree of variations in the light zone in the range of 100–500 μg g^{-1} H$_2$O. Most of garnet specimens from groups 2 and 3 do not show significant variations at the grain scale. An exception is sample ZTUv that shows a thin OH-enriched rim that correlates with a change in colour and an increase in Ti contents (Fig. 6df). Both core and rim are plotting close to the 1 : 1 cation exchange for H and Ti, indicating that the Ca$_3$Ti$_2$H$_2$Si$_2$O$_{12}$ endmember dominates in this sample. Zoning is also observed in the ZTAdr, in which garnet shows a complex oscillatory zoning (see Supplement S2).

5   Discussion

Garnets from all different rock types of the high-pressure area of the ZS including the rocks from the associated TGU were investigated, resulting in a wide diversity of garnet compositions and OH spectra. First, we discuss the relationships between garnet composition and the position of characteristic OH bands. The second part of the discussion is focused on the retention of OH under high-pressure and high-temperature (T) conditions. The effects of hydrogen diffusion processes over long timescales are also discussed comparing OH zoning patterns in garnet and H diffusion models. Finally, the contribution of garnet to the deep water cycle is quantified for the case of the Zermatt area.

5.1   Influence of composition on OH band position

As the samples experienced similar P–T conditions, with the possible exception of the garnet core of Z17TB03A, and garnet grew in a fluid-saturated environment (Reynes et al., 2020), the OH spectra and EPMA data can be used to study the effect of composition on the OH incorporation capacity and on the characterisation of OH defects in the garnet structure.

5.1.1   The influence of composition on garnet OH content

The garnet collection from the Zermatt–Saas area represents a great variety of compositions with various origins ranging from ultramafic rocks and mafic rocks (eclogites and garnet–diopside-rich rocks or mafic fels) to metasediments. Garnet group 3 (Ca^{2+}Fe^{3+} rich garnet specimens) contains the highest water content with up to 6000 μg g^{-1} H$_2$O (Table 3), followed by group 2 (Ca^{2+}Al^{3+}) with values up to 1800 μg g^{-1} H$_2$O. Garnet from group 1 (mostly composed of Fe^{2+}Al^{3+} garnet) contain fewer OH groups by 1 order of magnitude with values < 120 μg g^{-1} H$_2$O. In group 1, spessartine-rich garnet contains the highest H$_2$O content. There is an evident correlation between the Mn content of garnet in the spessartine nodule and the OH content (Fig. 3). In sample Z17TB07 the H$_2$O concentration profile follows the Mn zoning of the garnet (Fig. 7f). There is also a good correlation between H$_2$O and Ca contents in group 1 garnets. This result is supported by previous studies where Ca-rich garnet can contain up to several weight percent of H$_2$O (Amthauer and Rossman, 1998; Rossman and Aines, 1991), whereas pyrope–almandine garnets show at maximum a couple hundred micrograms per gram H$_2$O (Aines and Rossman, 1984). The grossular component in almandine garnet seems to enhance the capability of incorporating OH groups. Transects presented in Fig. 7 combined with their grossular content profile reveal that Ca-enriched zones are also enriched in H$_2$O. The same is observed with the maps of sample Z17TB04B. This trend is confirmed in Fig. 5 showing that for most analyses of group 1 the grossular content and the H$_2$O content are correlated.

For group 3, garnet grains from samples A4544 and B7415 show a water content of 500 μg g^{-1} H$_2$O, whereas the other samples for this group, ZTUv, ZTAdr and B2090, contain 4 to 10 times higher H$_2$O contents. Another anomaly appears in group 2 with sample ZTRod (350 μg g^{-1} H$_2$O) having 3 to 4 times less H$_2$O than samples ZTCarb and B7419. Figure 5b and d reveal a strong correlation between Ti content and H$_2$O incorporation in analysed garnets. Ti is known to control the OH incorporation in Ca-rich
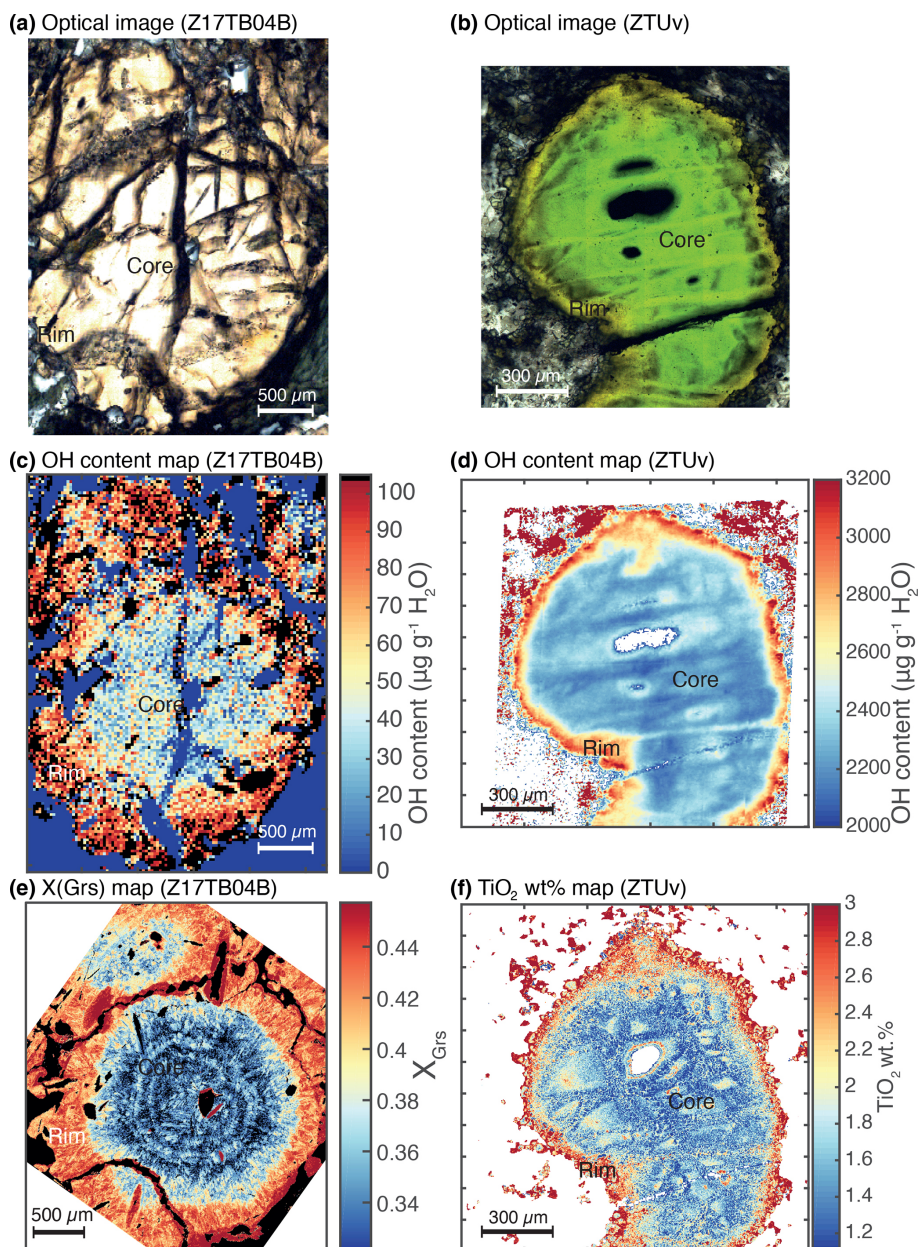
Figure 6. H_2O concentration map and selected X-ray map obtained on two garnet grains. **(a)** Optical image of a grain from sample Z17TB04B. **(b)** Optical image of a grain from sample ZTUv. **(c)** FTIR transmission map of H_2O content in garnet for the garnet grain from sample Z17TB04B. **(d)** Same as **(c)** but for sample ZTUv. **(e)** Compositional map (proportion of grossular endmember) for the selected grain of sample Z17TB04B. **(f)** Compositional map of TiO_2 of a ZTUv garnet grain.

garnet (Reynes et al., 2018). The general sequence of decreasing H_2O contents is Ti-rich andradite > Ti-rich grossular > grossular > andradite > spessartine > Ca-rich almandine > pyrope–almandine. This sequence coincides roughly with a decreasing unit-cell volume of garnet. Therefore, it is suggested that larger unit cells favour OH incorporation into garnet.

5.1.2 Interpretation of IR-band position for andradite-rich garnet of group 3

In garnet group 3, samples A4544 and B7415 show a very similar water content and spectrum shape (Fig. 4b). Their spectra only contain two bands, a main one at 3564–3566 cm^{-1} and a secondary one at 3604–3606 cm^{-1}. The main band is characteristic of OH in andradite garnet (Amthauer and Rossman, 1998) and was assigned to an iso-
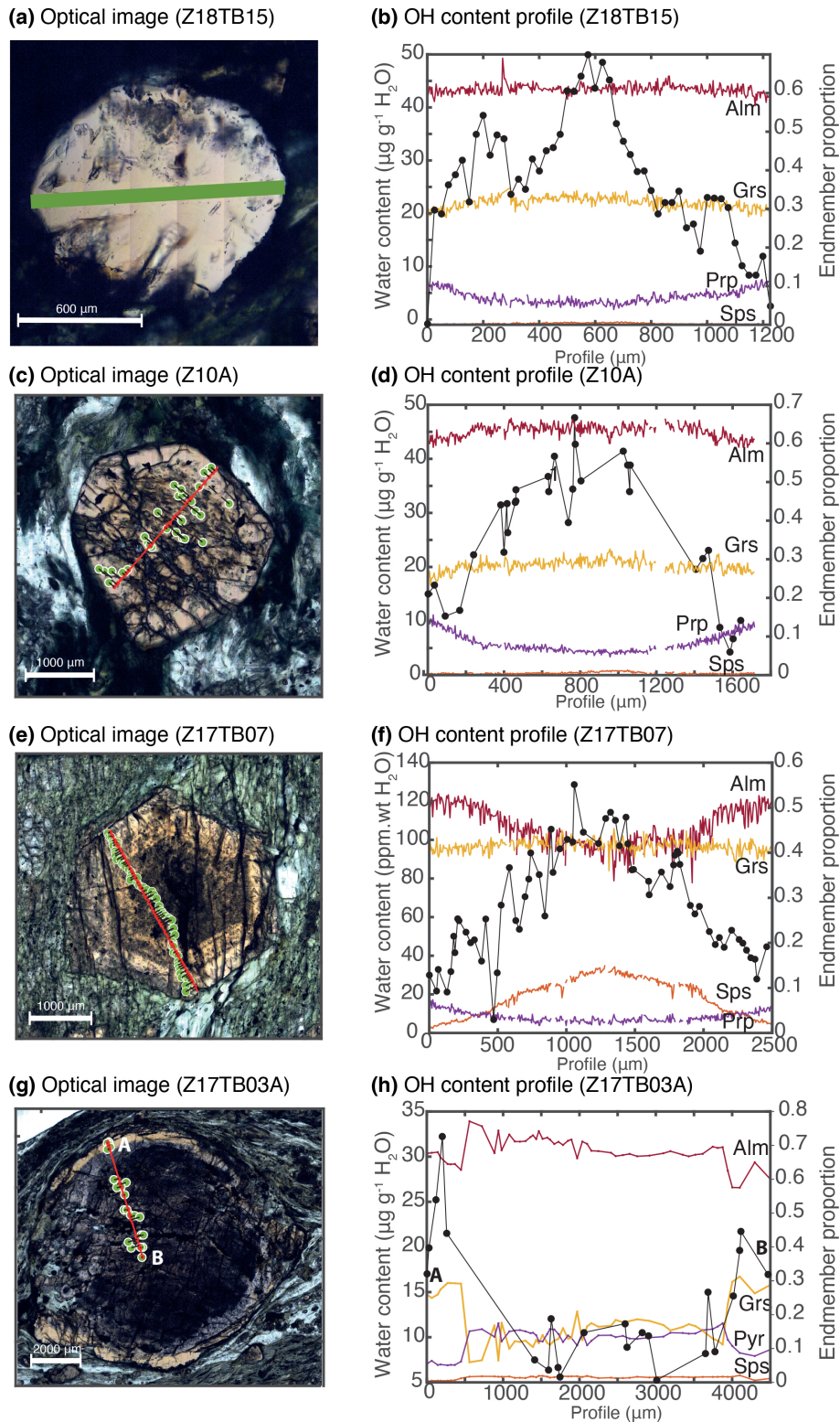
Figure 7. H_2O content profile and corresponding endmember proportion transects (X_{Alm}, X_{Grs}, X_{Pyr}, X_{Sps}) measured across single garnet grains. Spot positions are indicated by green dots and correspond to 25–50 μm spots. The red line corresponds to the linear regression of the spot position, on which spots are orthogonally projected to produce the adjusted profiles. This red line corresponds also to the compositional transect measured by EPMA. **(a)** Position on optical image of the transect acquired on a grain of sample Z18TB15. **(b)** Profile acquired with a step size of 25 μm and a spot size of 25 μm and endmember proportion profile extracted from a map (Fig. 2). Optical images **(c, e, g)** and adjusted profiles **(d, f, h)** of the grains analysed for samples Z10A, Z17TB07B and Z17TB03A. All OH profiles are expressed as micrograms per gram H_2O, and compositional transects reflect molar endmember proportions.

lated hydrogarnet substitution in andradite by Geiger and Rossman (2020a, b). This band is common to analyses from group 3 (highlighted by a green area in Fig. 4b) and the compositions of these garnets differ significantly, where sample B7415 is $Adr_{95}Grs_5$ and sample A4544 is $Adr_{75}Uv_{22}Grs_3$. This leads to two hypotheses: either Cr^{3+} has an effect very similar to Fe^{3+} on water incorporation or the OH groups are not in an environment with neighbouring Cr^{3+}. As there is a minor shift in the band position of about $2\,cm^{-1}$ that is negligible considering the difference in ionic radii of both Cr^{3+} (0.615 Å) and Fe^{3+} (0.645 Å), the second hypothesis is preferred.

The group 3 samples ZTUv, ZTAdr and B2090 have 4 to 10 times higher H_2O contents than group 1. The two main bands of samples A4544 and B7415, around 3560 and $3600\,cm^{-1}$, are still present. The positions are not the same: the first band is at $3557\,cm^{-1}$ for sample B2090, $3561\,cm^{-1}$ for ZTAdr and $3565\,cm^{-1}$ for ZTUv, while the second band position is at 3600, 3607 and $3605\,cm^{-1}$. Interestingly the second band is roughly at the same intensity as the first for samples ZTAdr and B2090. Additional bands are also present, such as a band at around $3576–3580\,cm^{-1}$ clearly identified on samples ZTU, ZTAdr and B2090 (highlighted by a red area in Fig. 4b). This band is not assigned to a specific point defect yet but is usually found in Ti-bearing andradites (Amthauer and Rossman, 1998; Armbruster et al., 1998; Geiger and Rossman, 2020b; Reynes et al., 2020). This band was identified as a major band of the Ti-bearing andradite in Reynes et al. (2020a), and its intensity appears to be strongly correlated with the amount of Ti. The band near $3563\,cm^{-1}$ also correlates with Ti. The three samples ZTUv, ZTAdr and B2090 show an H_2O content correlated with the amount of Ti (Fig. 5b) and a similar doublet at $3560–3580\,cm^{-1}$. Sample ZTUv even shows an H_2O-rich rim corresponding to a zone enriched in Ti (Fig. 5d, f). It can be suggested that this doublet corresponds to a special cluster of two hydrogen atoms in a silicon vacancy, charge balanced with two Ti^{4+} in close neighbouring octahedral sites (substitution $2Al^{3+} + Si^{4+} = 2Ti^{4+} + 2H^+$, $[Ti_2H_2]$ defect; see Reynes et al., 2020a). This interpretation requires the occurrence of coexisting point defects with 2H and 4H on a Si vacancy. Previous results for grossular (Cho and Rossman, 1993) using solid-state nuclear magnetic resonance showed that some crystals have 2H and 4H clusters which support this interpretation. The second main band at around $3600\,cm^{-1}$ and the minor bands at $3620\,cm^{-1}$ (sample ZTUv) and $3640\,cm^{-1}$ (samples ZTUv, ZTAdr, B2090) may be attributed to silicon vacancies in grossular in different environments at the atomic scale (see below).

5.1.3 Interpretation of IR-band position for grossular-rich garnet of group 2

In group 2, garnet compositions are dominated by grossular with minor andradite, almandine or uvarovite compo-

nents. The OH region of the spectrum can be divided into three domains: the main band at $3600–3623\,cm^{-1}$ (highlighted by an orange area in Fig. 4b), the high-wavenumber band at $3657\,cm^{-1}$ (yellow area in Fig. 4b), and the low-wavenumber broad band at $3550–3565\,cm^{-1}$ similar to the highlighted green area for andradite (Fig. 4b). The main band at around $3611\,cm^{-1}$ is characteristic of grossular (Rossman and Aines, 1991) and is attributed to a cluster containing two O_4H_4 in hydrogrossular by Geiger and Rossman (2020a). The exception is for some spectra of sample ZTRod type I showing a prominent $3621\,cm^{-1}$ band attributed by the same authors to three O_4H_4 clusters. Samples ZTRod type II, ZTCarb and B7419 all show two other bands at 3597–3598 and $3583\,cm^{-1}$. The first band is characteristic of grossular and is attributed to an isolated hydrogarnet substitution in a grossular local environment (Geiger and Rossman, 2020a). The second band at $3583\,cm^{-1}$ is linked to the presence of Ti in these garnets (see above). The EPMA analyses reveal that these specimens contain some minor amount of Ti (0.97 wt % TiO_2 for sample ZTCarb, 0.84 wt % TiO_2 for B7419, 0.29 wt % TiO_2 for ZTRod). This $3583\,cm^{-1}$ band is prominent in the case of samples B7419 and ZTCarb compared to ZTRod. B7419 and ZTCarb contain about twice the amount of TiO_2 present in ZTRod.

Garnet 35046 has a composition of $Grs_{41}Adr_{26}Uv_{31}$, and therefore the IR bands could be interpreted as resulting from the contribution of different environments. The spectrum of sample 35046 (Fig. 4b) presents two domains: a broad band centred at around $3550–3560\,cm^{-1}$ and an asymmetric band at $3617\,cm^{-1}$ with a shoulder at around $3600\,cm^{-1}$. The broad band contributes to around 33 % of the total absorbance and the asymmetric band of 66 %. Following the possible band assignment proposed above, the broad band might be attributed to isolated hydrogarnet substitution in an andradite environment, while the asymmetric band is assigned to two different clusters of interconnected hydrogarnet substitution in grossular.

The high-wavenumber band at $3657\,cm^{-1}$ is characteristic of natural and synthetic hydrogrossular (Rossman and Aines, 1991), and due to its proximity to a katoite OH band at $3660\,cm^{-1}$ (Geiger and Rossman, 2020a; Rossman and Aines, 1991), it has been proposed to be assigned to a "katoite-like" cluster consisting of six interconnected hydrogarnet substitutions (Geiger and Rossman, 2020a). However, the interpretation of these high-wavenumber bands remains controversial. These bands might represent multiple O_4H_4 clusters or alternatively might also be related to F–H exchange as highlighted by Mosenfelder et al. (2022).

5.1.4 Interpretation of IR-band position for almandine-rich garnet of group 1

The band assignment for this group is a bit more uncertain as IR bands are smaller and broader and not well defined (Fig. 4a). For this analysis, the case of sample ZTSps is ex-

cluded and will therefore be discussed in a separate section below. The analyses of group 1 present a broad band of absorption between 3460 and 3650 cm^{-1} (Fig. 4a). For all samples of this group, a prominent band is observed at 3550–3555 cm^{-1} (blue area in Fig. 4a) and is interpreted as being related to hydrogarnet substitution in almandine garnet (Aines and Rossman, 1984). This feature is observed for all analyses of this group. A large band appears at 3500 cm^{-1} only for a few spectra (samples Z10A core, Z17TB03A rim and Z17TB07 core). The presence of this band is correlated with Ca-enriched zones but does not show any absorption in bands related to grossular at 3600 cm^{-1}. Absorption in this domain (3500 cm^{-1}) was reported for almandine garnet (Aines and Rossman, 1984), but this feature is not assigned to any specific point defect yet. For some garnet zones, the absorption in the range of 3600–3650 cm^{-1} is even higher than for the almandine band (3550 cm^{-1}). These garnet specimens have high Ca contents that enhance the OH incorporation in almandine garnet (Fig. 5c).

5.1.5 Interpretation of IR-band position for almandine–spessartine solid solution (sample ZTSps)

The case of ZTSps is particular because garnet in this sample is dominated by spessartine (Sps$_{48-55}$, Table 2). Spessartine-rich garnet is known among pyralspites as being able to incorporate larger amount of OH (Aines and Rossman, 1984; Arredondo et al., 2001). The garnet specimens analysed here come from a manganese nodule, and the grain size is 1 order of magnitude smaller in comparison to other specimens (15–60 μm in diameter). The optical image (Fig. 3a) and the EPMA map of MnO (Fig. 3b) reveal two different zones: a dark zone composed of a 10–15 μm garnet grain with an enrichment in the almandine component (Alm$_{22}$) and a depletion in the spessartine component (Sps$_{48}$) compared to a light zone (Sps$_{55}$Alm$_{18}$). The light zone contains bigger grains, on average around 50–60 μm. As observed on the EPMA map (Fig. 3b) the single grains appear to be zoned. In the low-Mn zone, a single band is measured centred at 3554 cm^{-1}. This band is either attributed to hydrogarnet substitution in an almandine environment or a small andradite component (Adr$_9$). For the high-Mn zone, the bands at higher wavenumbers increase significantly (Fig. 3c). The two new bands at 3591 and 3640 cm^{-1} present higher absorption intensities (25 % higher intensity for the 3640 cm^{-1} band compared to the 3560 cm^{-1} band). These bands were previously identified in almandine–spessartine garnet (Aines and Rossman, 1984) with the same "wide" shape but were not clearly attributed to any point defect.
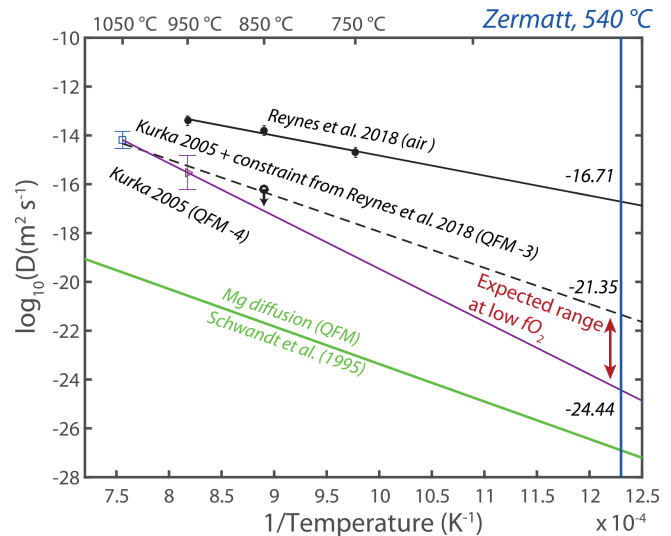

Figure 8. Arrhenius plot representing hydrogen diffusion rates in grossular from the studies of Kurka (2005) and Reynes et al. (2018). The diffusivities are linearly extrapolated to the determined temperature of the metamorphic peak in Zermatt: 540 °C (Angiboust et al., 2009). See text for details. The Mg cation diffusion line at QFM plotted in green is from Schwandt et al. (1995).

5.2 Retention of hydrogen in garnet under high-pressure conditions

All samples of garnet analysed in this study have an OH content from a few tens to 5000 μg g^{-1} H$_2$O. The widespread zoning of H$_2$O and garnet compositions raises two key questions: when was H$_2$O incorporated into garnet and how can it be preserved? Transects and maps of both major-element chemistry (EPMA) (Figs. 2, 3, 6, 7) and OH content (FTIR) (Figs. 3, 6, 7) reveal that OH zoning is intimately correlated to major and minor element zoning and can therefore be interpreted as a growth feature. Among garnet of group 1, the detailed transects exhibit two different trends. Samples Z18TB15, Z10A and Z17TB07 show a core with a higher concentration of H$_2$O than the rim. On the other hand, samples Z17TB04B and Z17TB03A show more H$_2$O in the rim than the core. Sample Z17TB03A shows very low H$_2$O contents in the core and an increase toward the rim. This observed variability and the complex zoning have three main implications:

1. Garnet growth in subducted rocks is generally related to dehydration reactions or to the presence of external fluids (e.g. Baxter and Caddick, 2013; Vho et al., 2020). In both cases the activity of H$_2$O is close to unity as an aqueous fluid is produced by the garnet-forming reaction. The amount of OH incorporated in garnet during growth seems to be rather controlled by the chemical composition of the stable garnet, which is a function of P–T conditions and

the reactive bulk rock composition (e.g. Lanari et al., 2017). Additionally, the water fugacity is also a function of P–T, and thus complex zoning patterns are expected. As the samples shared the same P–T evolution, the first-order ability for garnet to incorporate H_2O in the order Ti-rich andradite > Ti-rich grossular > grossular > andradite > spessartine > Ca-rich almandine > pyrope–almandine is related to the bulk rock system, which has a direct impact on garnet's ability to create suitable point defects for incorporating the OH groups. This is also supported by the observation that the spectrum shape varies across the different zones (Fig. 4), which means that the OH groups are sitting in slightly different environments.

2. The OH zoning pattern produced during growth is not significantly affected by diffusion afterwards, indicating a lack of re-equilibration of H under these conditions as is also the case for the major and minor elements. Figure 8 displays a range of hydrogen diffusivity values obtained in previous studies for grossular garnet (Kurka, 2005; Reynes et al., 2018). These studies revealed that the hydrogen diffusion in air is rapid and is related to an oxidation mechanism $\left(\left\{M^{2+} + H^+\right\} + \frac{1}{4}O_2 = M^{3+} + \frac{1}{2}H_2O\right)$, whereas the diffusion rates slow down by several orders of magnitude at lower oxygen fugacity. The extrapolation of hydrogen diffusion rates in air at the temperature of $540 \pm 20\,°C$ corresponding to the temperature under peak pressure conditions recorded in the Zermatt–Saas zone (Angiboust et al., 2009) gives a value of $\log(D[\mathrm{m^2\,s^{-1}}]) = -16.7 \pm 0.26$. Note that "$\log(D[\mathrm{m^2\,s^{-1}}])$" is formally $\log(D[\mathrm{m^2\,s^{-1}}]/1\,\mathrm{m^2\,s^{-1}})$, as the argument of a logarithm is dimensionless. For extrapolation under low-oxygen-fugacity conditions, a range of diffusivity was computed based on two data points from Kurka (2005) with and without the low-oxygen-fugacity constraint from Reynes et al. (2018). The range of $\log(D[\mathrm{m^2\,s^{-1}}])$ values for the temperature of the pressure peak is estimated between -21.4 ± 0.46 and -24.4 ± 0.67. These three $\log(D[\mathrm{m^2\,s^{-1}}])$ estimates were then used for modelling hydrogen diffusion in 2D for a representative sample of almandine-rich garnet (group 1). Sample Z17TB07 was selected as it shows very distinct zoning patterns. The starting conditions (initial in Fig. 9) were set using sharp water zoning assumed to represent three distinct stages of garnet growth and is based on the zoning patterns observed in the chemical maps (Fig. 2b). The model simulates diffusion for a duration of 4 Myr – corresponding to the maximum estimated time spent under high-pressure conditions – using the three different diffusion rates. The model at $\log(D[\mathrm{m^2\,s^{-1}}]) = -16.7$ shows a very fast loss of H_2O and a nearly total re-equilibration

within 500 years (Fig. 9a) assuming dry boundary conditions. Experiments at $\log(D[\mathrm{m^2\,s^{-1}}]) = -21.4$ show that the initial concentration in the core of the garnet is preserved in 4 Myr (Fig. 9b), but the intermediate zones are blurred and the boundaries no longer visible. With the lowest diffusion coefficient of $\log(D[\mathrm{m^2\,s^{-1}}]) = -24.4$, H_2O zoning is fully preserved (Fig. 9c). The only observable effect is a $\sim 50\,\mu m$ wide blurring transition between the initially sharp zones. The OH zoning patterns observed in garnet from the Zermatt–Saas area suggest, based on the results of diffusion modelling, that diffusion of H was slow with $\log(D[\mathrm{m^2\,s^{-1}}])$ values in the range of -21.4 to -24.4. Due to the lack of experiments at high pressure, it is unclear if this is related to oxygen fugacity or other factors. Figure 4 reveals that the IR-band positions and intensities vary for the different garnet zoning patterns. As discussed above, it is likely that different point defects – or at least different environments at the atomic scale – co-exist in a single grain. It is suggested that these different OH groups follow different diffusion pathways. A substitution mechanism involving coupled substitution and local charge equilibration like with Ti ($2M^{3+} + Si^{4+} = 2Ti^{4+} + 2H^+$) (Reynes et al., 2020) could also influence the stability of OH groups in the garnet structure.

3. The preserved OH zoning patterns also mean that H_2O contents that were acquired during prograde garnet growth are preserved. For the almandine-rich garnets the prograde cores have generally higher OH contents than the mantle and the rims indicating that increasing pressure does not necessarily lead to higher OH contents (see Sect. 5.3). The case of sample Z17TB03A is particularly interesting because the nearly dry core of this garnet is interpreted to have formed at pre-Alpine times under amphibolite-facies conditions (Bucher et al., 2019), whereas the rim containing OH formed during Alpine metamorphism at higher pressure (Bovay et al., 2022; Bucher et al., 2019). In the spessartine-rich samples, the early-formed parts highest in Mn have the highest OH contents, whereas the recrystallisation zones have lower OH contents. Finally, the ZTUv sample containing andradite–uvarovite comes from metasomatised mafic dyke in the serpentinites. The core of this garnet might have already formed during the oceanic alteration, whereas the rim that is higher in Ti and OH contents is interpreted to be related to the eclogite-facies equilibration and fluid flow when the serpentinites experienced the fluid-liberating reaction of antigorite + brucite to olivine + chlorite + fluid close to peak metamorphic conditions (Kempf et al., 2020).
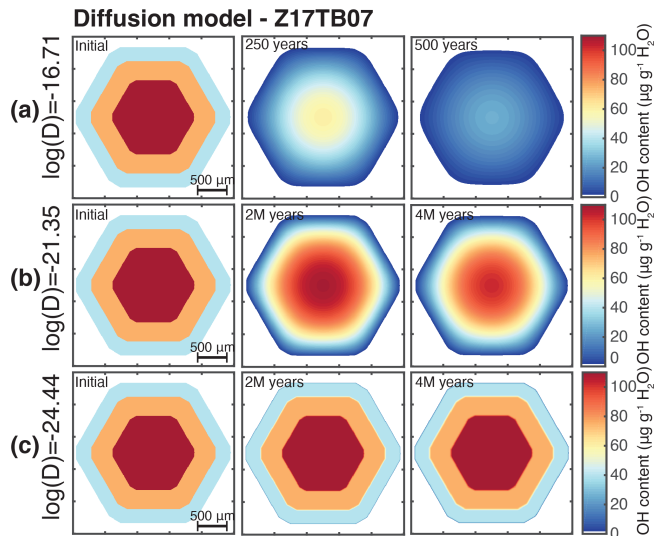
Figure 9. Hydrogen diffusion modelling for a grain of sample Z17TB07 at metamorphic peak temperature (540 °C) for three different diffusivity values and at three different time steps. **(a)** H diffusion modelling with $\log(D[\mathrm{m^2\,s^{-1}}]) = -16.71$ at initial stage and after 250 and 500 years. **(b)** H diffusion modelling with $\log(D[\mathrm{m^2\,s^{-1}}]) = -21.35$ at initial stage and after 2 and 4 Myr. **(c)** Same as **(b)** but with $\log(D[\mathrm{m^2\,s^{-1}}]) = -24.44$.

5.3 Comparison with other high-pressure garnets

The retention of hydrogen in garnet under high-pressure conditions was observed in other locations. Eclogitic garnet from the Kockchetav massif has undergone ultra-high-pressure conditions (up to 6.0 GPa, 1000 °C; Okamoto, 2000) and shows a gradual increase in H_2O content with the metamorphic grade: 10–50 µg g^{-1} H_2O for quartz-bearing eclogites, 80–120 µg g^{-1} H_2O for coesite-bearing eclogites and 130–150 µg g^{-1} H_2O for diamond-grade eclogites (Katayama et al., 2006). Samples from the Erzgebirge massif show H_2O contents in eclogitic garnet in the range of 43–84 µg g^{-1} H_2O and 121–241 µg g^{-1} H_2O in garnetite (metarodingite) (Schmädicke and Gose, 2020; Gose and Schmädicke, 2018; Schmädicke and Gose, 2017). Garnet from the Lepontine Alps (Cima Di Gagnone and Alpe Arami) is the most H_2O-depleted high-pressure garnet reported with 4–11 µg g^{-1} H_2O in eclogites and 23–46 µg g^{-1} H_2O in garnetite (Schmädicke and Gose, 2020). Ultra-high-pressure pyrope from the Dora-Maira whiteschists contains 10–30 µg g^{-1} H_2O (Blanchard and Ingrin, 2004a; Rossman et al., 1989). Water contents of 14–1900 µg g^{-1} H_2O are reported in eclogitic garnet from Dabie-Sulu (Chen et al., 2007; Sheng et al., 2007; Xia et al., 2005), which is an H_2O content about 3 orders of magnitude higher than in other localities. In those studies, all spectra evaluated with high H_2O contents present a broad band centred on 3400 cm^{-1} (Chen et al., 2007; Sheng et al., 2007; Xia et al., 2005) that might be attributed to fluid inclusion or non-structural water (Reynes

et al., 2020) or even to micro-inclusions of chlorite (Gou et al., 2020). It is therefore likely that these studies overestimated the amount of OH incorporated in garnet.

One important question regarding the variability in H_2O contents in garnet is whether the composition controlled by P and T is the main factor or whether a direct pressure effect exists in addition. The OH contents measured in eclogitic garnet in Zermatt, for example Z17TB07, with 50–110 µg g^{-1} H_2O appears to be slightly higher than in Kockchetav and Erzgebirge quartz–eclogite garnet. One of the hypotheses suggested for the increasing OH content in garnet with pressure is based on the increasing Ca content in garnet with pressure (Schmädicke and Gose, 2017). The peak metamorphic conditions of Zermatt are within the domain of quartz-bearing eclogites. Many Ca-bearing phases, like zoisite or amphibole, are still present in the matrix of these rocks. If such rocks were buried deeper, it is likely that these hydrous phases would eventually break down and lead to the formation of more grossular (Ca-rich) garnet. As previously discussed, it appears that the Ca component influences the H uptake of garnet (Fig. 5). This mechanism could be seen as an indirect effect of pressure on OH incorporation. On the other hand, Lu and Keppler (1997) showed experimentally that OH solubility in natural Dora-Maira pyrope at 1000 °C increases with pressure in the range of 1.5 to 10.0 GPa. This enhanced solubility of the OH group with pressure is important when considering the subduction geotherms. In a cold subduction environment, hydrous phases like lawsonite and phengite could take H_2O down to 200 km depth (100 kbar, 800 °C; Schmidt and Poli, 1998) where these phases will eventually break down, likely leading to garnet with significantly higher H_2O contents. By contrast, in warm subduction settings amphibole breakdown occurs at 80 km depth (30 kbar, 600 °C) and the solubility of H in garnet will be lower. Based on pyrope the difference in solubility could be up to a factor of 2.5 (Lu and Keppler, 1997).

5.4 Water budget for the Zermatt subducted oceanic lithosphere

In this study, the H_2O contents of garnet were determined for each of the rock types that are typical for a slice of high-pressure crust of the Zermatt–Saas area. By estimating the volume of the different units of the slice and the volume of garnet in each of them, it is possible to estimate the total amount of water stored in garnet under these quartz–eclogite-facies conditions. For the computation, a unit volume of 2.2 km × 1.5 cm × 1 km is considered. The value of 2.2 km corresponds to the estimated thickness of the slab, composed of 1 km ultramafic rocks, 1 km mafic rocks (eclogitic mafic fels) and 200 m of sedimentary cover. The value of 1.5 cm represents the amount of crust passing under these conditions in 1 year, based on a plate movement rate of 1.5 cm yr^{-1} (Handy et al., 2010). The value of 1 km corresponds to a lateral section of slab. If the length of the sub-
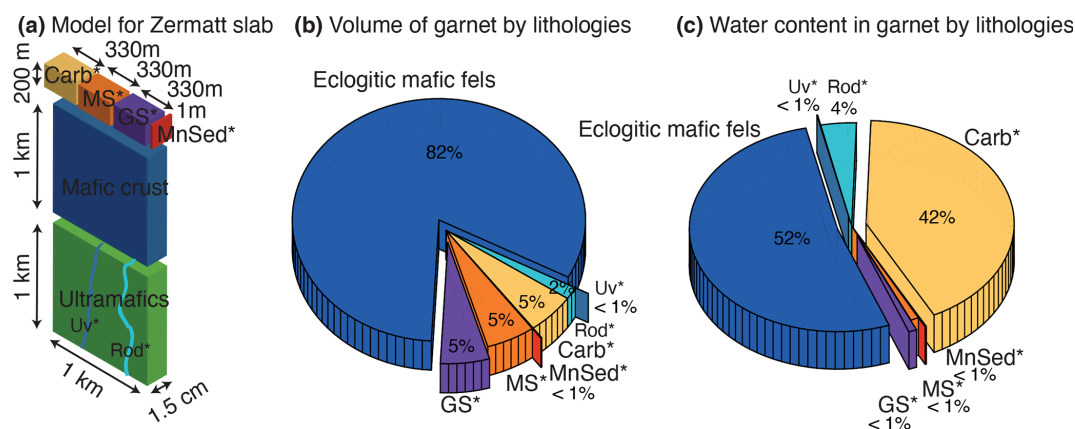
Figure 10. Water budget in garnet for the deeply subducted oceanic lithosphere preserved in the Zermatt area. **(a)** Model of lithology and unit partitioning in the Zermatt area. **(b)** Pie chart representing the relative volume of garnet by lithology. **(c)** Pie chart highlighting the relative water contribution of garnet from different rock units. Abbreviations: Carb* is metacarbonates, MS* is mafic schists, GS* is garnet schists, MnSed* is Mn-rich metasediments, Rod* is rodingites and Uv* is andradite–uvarovite veins.

Table 4. Parameters and quantities used for the computation of water budget in garnet of the Zermatt area.

	Ultramafics		Mafic crust	Sedimentary cover			
	Rodingite	Uv / Adr	Mafic fels	Grt schist	Mafic schist	Mn Sed	MetaCarb
Volume Grt-bearing rock (%)	0.01	0.0001	100	33	33	1	33
Grt proportion (%)	60	20	30	30	20	90	30
Density ($kg\,m^{-3}$)	3600	3800	3900	4000	4000	4070	3645
Garnet water content (wt %)	0.04	0.24	0.01	0.0015	0.0025	0.02	0.13

Mn Sed is Mn-rich metasediments. MetaCarb is metacarbonates.

duction zone is known, then a flow (in $kg\,yr^{-1}$ of H_2O) can be determined. Results including the percentage of the different garnet-bearing rocks, their garnet volume fractions and the corresponding total amount of H_2O stored in garnet are presented in Table 4. The sedimentary layer is subdivided into four components: 33 vol % garnet schists, 33 % metacarbonates, 33 % mafic schist and 1 % spessartine nodules (Fig. 10a.). The relative volumes of garnet and the corresponding proportion of H_2O are summarised in Fig. 10b and c. The eclogitic mafic fels contains the largest volume of garnet with 82 vol % of all garnet (Fig. 10b). Garnets from metasediments are responsible for 15 vol %, roughly equilibrated between the three main rock types (mafic schists, garnet schists and metacarbonates). Rodingites and andradite veins represent less than 3 vol % of the total garnet volume, as they only sporadically occur in small boudins and dykes in the serpentinites. For garnet in the Zermatt–Saas area, the total amount of water contained in the form of structural OH groups is 3360 $kg\,H_2O\,km^{-1}\,yr^{-1}$. Considering the 1 km thick slice of serpentinites and an average of 25 % metamorphic olivine (growing after brucite–antigorite dehydration reaction) containing 100 $\mu g\,g^{-1}\,H_2O$ (Kempf et al., 2020), the water stored in metamorphic olivine is about 1125 $kg\,km^{-1}\,yr^{-1}$. These calculations show that at the depth

reached by the Zermatt–Saas slice ($\sim 80\,km$) garnet can carry 3 times more water than metamorphic olivine. The water stored in garnet and olivine can potentially be transported deeper in the Earth beyond the disappearance of both antigorite and chlorite. In terms of water partitioning between the different lithologies, it appears that the eclogitic mafic fels contains 52 vol % of the total water (Fig. 10c) and the metacarbonates 42 vol %. Therefore, eclogitic mafic fels and metacarbonates play a major role in the deep water cycle, even though the H_2O content in eclogitic garnet is rather small at $\sim 100\,\mu g\,g^{-1}\,H_2O$. For metacarbonates, the volume is small (5 vol %), but garnet has very high water contents ($> 1000\,\mu g\,g^{-1}\,H_2O$). Other sediments, like mafic schists and garnet schists, are contributing to less than 3 % due to both their small relative rock volume and the low H_2O contents in garnet ($< 50\,\mu g\,g^{-1}\,H_2O$). Rodingite garnets contribute 4 % of the garnet water budget. Their relatively small rock volume associated with the high garnet water contents ($400\,\mu g\,g^{-1}\,H_2O$) explains why this unit has a minor contribution of garnet to the deep water cycle. It is important to note that the garnet samples showing the highest water content (andradite or group 3 garnets with 5000 $\mu g\,g^{-1}\,H_2O$) are a negligible part ($\ll 1$ %) of this budget due to their small relative rock volume. These calculations are restricted only to

garnet and thus represent a minimum amount of H_2O transported beyond sub-arc depth in subduction zones. Clinopyroxene is likely to contain higher H_2O contents than garnet, and additional studies are needed to quantify its contribution.

6   Conclusions

The detailed investigation of H_2O incorporation into garnet with different compositions in various eclogite-facies rocks from the Zermatt–Saas area revealed important systematics for the garnet deep water cycle at multiple scales.

– At the metre to kilometre scale, the amount of water taken up in garnet would be controlled by eclogitic garnets despite their relatively low water contents and by carbonate-rich metasediments despite their relatively small volume.

– At the microscale, OH zoning was observed within single grains. These zoning patterns reveal a strong correlation between the major-element composition and OH content. The Ca, Mn and Ti components are driving the capability of garnet to incorporate OH groups. The zoning is preserved and therefore did not significantly re-equilibrate by diffusion after growth, suggesting very low diffusivities of hydrogen under eclogite- and blueschist-facies conditions.

– At the atomic scale, it was possible to assign different infrared bands to specific point defects. The observed bands are witnessing the local environment of the OH groups and provide information about the immediate environment of the OH groups. This study supports that in a single garnet grain, several hydrous nano-scale domains are co-existing: hydrogarnet in grossular, andradite and almandine domains and Ti_2H_2 point defects. Some of the measured spectra show high-frequency bands (3640–$3660\,cm^{-1}$), for which the interpretation remains controversial (interconnected hydrogarnet substitutions or F–H defect).

References

Agard, P., Monié, P., Jolivet, L., and Goffé, B.: Exhumation of the Schistes Lustrés complex: in situ laser probe $^{40}Ar / ^{39}Ar$ constraints and implications for the Western Alps, J. Metamorph. Geol., 20, 599–618, https://doi.org/10.1046/j.1525-1314.2002.00391.x, 2002.

Aines, R. D. and Rossman, G. R.: The hydrous component in garnets: pyralspites, Am. Mineral., 69, 1116–1126, 1984.

Amato, J. M., Johnson, C. M., Baumgartner, L. P., and Beard, B. L.: Rapid exhumation of the Zermatt-Saas ophiolite deduced from high-precision SmNd and RbSr geochronology, Earth Planet. Sc. Lett., 171, 425–438, https://doi.org/10.1016/S0012-821X(99)00161-2, 1999.

Amthauer, G. and Rossman, G. R.: The hydrous component in andradite garnet, Am. Mineral., 83, 835–840, https://doi.org/10.2138/am-1998-7-815, 1998.

Andrut, M., Wildner, M., and Beran, A.: The crystal chemistry of birefringent natural uvarovites, Part IV. OH defect incorporation mechanisms in non-cubic garnets derived from

polarized IR spectroscopy, Eur. J. Mineral., 14, 1019–1026, https://doi.org/10.1127/0935-1221/2002/0014-1019, 2002.

Angiboust, S., Agard, P., Jolivet, L., and Beyssac, O.: The Zermatt-Saas ophiolite: the largest (60-km wide) and deepest (c. 70–80 km) continuous slice of oceanic lithosphere detached from a subduction zone?, Terra Nova, 21, 171–180, https://doi.org/10.1111/j.1365-3121.2009.00870.x, 2009.

Armbruster, T., Birrer, J., Libowitzky, E., and Beran, A.: Crystal chemistry of Ti-bearing andradites, Eur. J. Mineral., 10, 907–922, https://doi.org/10.1127/ejm/10/5/0907, 1998.

Arredondo, E. H., Rossman, G. R., and Lumpkin, G. R.: Hydrogen in spessartine-almandine garnets as a tracer of granitic pegmatite evolution, Am. Mineral., 86, 485–490, https://doi.org/10.2138/am-2001-0412, 2001.

Basso, R., Cimmino, F., and Messiga, B.: Crystal-chemistry of hydrogarnets from 3 different microstructural sites of a basaltic metarodingite from the Voltri-massif (Western Liguria, Italy), Neues Jahrb. Mineral.-Abh., 148, 246–258, 1984.

Baxter, E. F. and Caddick, M. J.: Garnet growth as a proxy for progressive subduction zone dehydration, Geology, 41, 643–646, https://doi.org/10.1130/G34004.1, 2013.

Bearth, P.: Die Ophiolithe der Zone von Zermatt-Saas Fee, Kümmerly and Frey, Bern, 1967.

Bell, D. R., Ihinger, P. D., and Rossman, G. R.: Quantitative analysis of trace OH in garnet and pyroxenes, Am. Mineral., 80, 465–474, https://doi.org/10.2138/am-1995-5-607, 1995.

Blanchard, M. and Ingrin, J.: Hydrogen diffusion in Dora Maira pyrope, Phys. Chem. Miner., 31, 593–605, https://doi.org/10.1007/s00269-004-0421-z, 2004a.

Blanchard, M. and Ingrin, J.: Kinetics of deuteration in pyrope, Eur. J. Mineral., 16, 567–576, https://doi.org/10.1127/0935-1221/2004/0016-0567, 2004b.

Bovay, T., Rubatto, D., and Lanari, P.: Pervasive fluid-rock interaction in subducted oceanic crust revealed by oxygen isotope zoning in garnet, Contrib. Mineral. Petrol., 176, 55, https://doi.org/10.1007/s00410-021-01806-4, 2021.

Bovay, T., Lanari, P., Rubatto, D., Smit, M., and Piccoli, F.: Pressure–temperature–time evolution of subducted crust revealed by complex garnet zoning (Theodul Glacier Unit, Switzerland), J. Metamorph. Geol., 40, 175–206, https://doi.org/10.1111/jmg.12623, 2022.

Bowtell, S. A., Cliff, R. A., and Barnicoat, A. C.: Sm-Nd isotopic evidence on the age of eclogitization in the Zermatt-Saas ophiolite, J. Metamorph. Geol., 12, 187–196, https://doi.org/10.1111/j.1525-1314.1994.tb00013.x, 1994.

Bucher, K., Fazis, Y., De Capitani, C., and Grapes, R.: Blueschists, eclogites, and decompression assemblages of the Zermatt-Saas ophiolite: High-pressure metamorphism of subducted Tethys lithosphere, Am. Mineral., 90, 821–835, 2005.

Bucher, K., Weisenberger, T. B., Klemm, O., and Weber, S.: Decoding the complex internal chemical structure of garnet porphyroblasts from the Zermatt area, Western Alps, J. Metamorph. Geol., 37, 1151–1169, https://doi.org/10.1111/jmg.12506, 2019.

Chen, R.-X., Zheng, Y.-F., Gong, B., Zhao, Z.-F., Gao, T.-S., Chen, B., and Wu, Y.-B.: Origin of retrograde fluid in ultrahigh-pressure metamorphic rocks: Constraints from mineral hydrogen isotope and water content changes in eclogite–gneiss transitions in the Sulu orogen, Geochim. Cosmochim. Ac., 71, 2299–2325, https://doi.org/10.1016/j.gca.2007.02.012, 2007.

Chinner, G. A. and Dixon, J. E.: Some High-pressure Parageneses of the Allalin Gabbro, Valais, Switzerland, J. Petrol., 14, 185–202, https://doi.org/10.1093/petrology/14.2.185, 1973.

Cho, H. and Rossman, G. R.: Single-crystal NMR studies of low-concentration hydrous species in minerals: Grossular garnet, Am. Mineral., 78, 1149–1164, 1993.

Cohen-Addad, C., Ducros, P., and Bertaut, E. F.: Etude de la Substitution du groupement SiO_4 par $(OH)_4$ dans les composés $Al_2Ca_3(OH)_{12}$ et $Al_2Ca_3(SiO_4)_{2.16}(OH)_{3.36}$ de type grenat, Acta Crystallogr., 23, 220–230, 1967.

Crank, J.: The Mathematics of diffusion, Clarendon–Oxford university press, ISBN: 0 19 853344 6, 1975.

Foreman, D. W.: Neutron and X-Ray Diffraction Study of $Ca_3Al_2(O_4D_4)_3$, a Garnetoid, J. Chem. Phys., 48, 3037–3041, https://doi.org/10.1063/1.1669569, 1968.

Freeze, R. A. and Cherry, J. A.: Groundwater, Prentice-Hall, Englewood Cliffs, N.J. 07632, ISBN: 0-13-365312-9, 604 pp., 1979.

Geiger, C. A. and Rossman, G. R.: Micro- and nano-size hydrogarnet clusters and proton ordering in calcium silicate garnet: Part I. The quest to understand the nature of "water" in garnet continues, Am. Mineral., 105, 455–467, https://doi.org/10.2138/am-2020-7256, 2020a.

Geiger, C. A. and Rossman, G. R.: Micro- and nano-size hydrogarnet clusters in calcium silicate garnet: Part II. Mineralogical, petrological, and geochemical aspects, Am. Mineral., 105, 468–478, https://doi.org/10.2138/am-2020-7257, 2020b.

Geiger, C. A., Langer, K., Bell, D. R., Rossman, G. R., and Winkler, B.: The hydroxide component in synthetic pyrope, Am. Mineral., 76, 49–59, 1991.

Gose, J. and Schmädicke, E.: Water Incorporation in Garnet: Coesite versus Quartz Eclogite from Erzgebirge and Fichtelgebirge, J. Petrol., 59, 207–232, https://doi.org/10.1093/petrology/egy022, 2018.

Gou, Y., Wang, Q., Li, Y., and Wirth, R.: Water Content in Garnet from Eclogites: Implications for Water Cycle in Subduction Channels, Minerals, 10, 410, https://doi.org/10.3390/min10050410, 2020.

Handy, M. R., M. Schmid, S., Bousquet, R., Kissling, E., and Bernoulli, D.: Reconciling plate-tectonic reconstructions of Alpine Tethys with the geological–geophysical record of spreading and subduction in the Alps, Earth-Sci. Rev., 102, 121–158, https://doi.org/10.1016/j.earscirev.2010.06.002, 2010.

Katayama, I., Nakashima, S., and Yurimoto, H.: Water content in natural eclogite and implication for water transport into the deep upper mantle, Lithos, 86, 245–259, 2006.

Kempf, E. D., Hermann, J., Reusser, E., Baumgartner, L. P., and Lanari, P.: The role of the antigorite + brucite to olivine reaction in subducted serpentinites (Zermatt, Switzerland), Swiss J. Geosci., 113, 16, https://doi.org/10.1186/s00015-020-00368-0, 2020.

Khomenko, V. M., Langer, K., Beran, A., Koch-Müller, M., and Fehr, T.: Titanium substitution and OH-bearing defects in hydrothermally grown pyrope crystals, Phys. Chem. Miner., 20, 483–488, https://doi.org/10.1007/BF00203218, 1994.

Kühberger, A., Fehr, T., Huckenholz, H. G., and Amthauer, G.: Crystal chemistry of a natural schorlomite and Ti-andradites synthesized at different oxygen fugacities, Phys. Chem. Miner., 16, 734–740, https://doi.org/10.1007/BF00209694, 1989.

Kurka, A.: Hydrogen in Ca-rich garnets: diffusion and stability of OH-defects, PhD thesis, Toulouse III Paul Sabatier, Toulouse, France, 371 pp., 2005.

Kurka, A., Blanchard, M., and Ingrin, J.: Kinetics of hydrogen extraction and deuteration in grossular, Mineral. Mag., 69, 359–371, https://doi.org/10.1180/0026461056930257, 2005.

Lager, G. A., Armbruster, T., and Faber, J.: Neutron and X-ray diffraction study of hydrogarnet $Ca_3Al_2(O_4H_4)_3$, Am. Mineral., 72, 756–765, 1987.

Lanari, P., Vidal, O., De Andrade, V., Dubacq, B., Lewin, E., Grosch, E. G., and Schwartz, S.: XMapTools: A MATLAB© – based program for electron microprobe X-ray image processing and geothermobarometry, Comput. Geosci., 62, 227–240, https://doi.org/10.1016/j.cageo.2013.08.010, 2014.

Lanari, P., Giuntoli, F., Loury, C., Burn, M., and Engi, M.: An inverse modeling approach to obtain $P-T$ conditions of metamorphic stages involving garnet growth and resorption, Eur. J. Mineral., 29, 181–199, https://doi.org/10.1127/ejm/2017/0029-2597, 2017.

Lanari, P., Vho, A., Bovay, T., Airaghi, L., and Centrella, S.: Quantitative compositional mapping of mineral phases by electron probe micro-analyser, in: Metamorphic Geology: Microscale to Mountain Belts, Vol. 478, edited by: Ferrero, S., Lanari, P., Goncalves, P., and Grosch, E. G., Geological Society of London, Special Publications, https://doi.org/10.1144/SP478.4, 2019.

Lemoine, M., Bas, T., Arnaud-Vanneau, A., Arnaud, H., Dumont, T., Gidon, M., Bourbon, M., de Graciansky, P.-C., Rudkiewicz, J.-L., Megard-Galli, J., and Tricart, P.: The continental margin of the Mesozoic Tethys in the Western Alps, Mar. Pet. Geol., 3, 179–199, https://doi.org/10.1016/0264-8172(86)90044-9, 1986.

Li, X.-P., Rahn, M., and Bucher, K.: Serpentinites of the Zermatt-Saas ophiolite complex and their texture evolution, J. Metamorph. Geol., 22, 159–177, https://doi.org/10.1111/j.1525-1314.2004.00503.x, 2004.

Lu, R. and Keppler, H.: Water solubility in pyrope to 100 kbar, Contrib. Mineral. Petrol., 129, 35–42, https://doi.org/10.1007/s004100050321, 1997.

Luoni, P., Rebay, G., Spalla, M. I., and Zanoni, D.: UHP Ti-chondrodite in the Zermatt-Saas serpentinite: Constraints on a new tectonic scenario, Am. Mineral., 103, 1002–1005, https://doi.org/10.2138/am-2018-6460, 2018.

Maldener, J., Hösch, A., Langer, K., and Rauch, F.: Hydrogen in some natural garnets studied by nuclear reaction analysis and vibrational spectroscopy, Phys. Chem. Miner., 30, 337–344, https://doi.org/10.1007/s00269-003-0321-7, 2003.

Martin, S., Rebay, G., Kienast, J.-R., and Mével, C.: An eclogitised oceanic palaeo-hydrothermal field from the St. Marcel Valley (Italian Western Alps), Ofioliti, 33, 49–63, 2008.

Mosenfelder, J. L., von der Handt, A., Withers, A. C., Bureau, H., Raepsaet, C., and Rossman, G. R.: Coupled hydrogen and fluorine incorporation in garnet: New constraints from FTIR, ERDA, SIMS, and EPMA, Am. Mineral., 107, 587–602, https://doi.org/10.2138/am-2021-7880, 2022.

Nace, R. L.: Scientific framework of world water balance, United Nations Educational, Scientific and Cultural Organization, SC.70/XXI.7/A, https://unesdoc.unesco.org/ark:/48223/pf0000073095 (last access: 10 July 2023), 1971.

Okamoto, K. L.: Petrological study of the diamond grade eclogite in the Kokchetav massif, northern Kazakhstan, Isl. Arc, 9, 379–399, 2000.

Peacock, S. M.: Fluid Processes in subduction Zones, Science, 248, 329–337, https://doi.org/10.1126/science.248.4953.329, 1990.

Rebay, G., Zanoni, D., Langone, A., Luoni, P., Tiepolo, M., and Spalla, M. I.: Dating of ultramafic rocks from the Western Alps ophiolites discloses Late Cretaceous subduction ages in the Zermatt-Saas Zone, Geol. Mag., 155, 298–315, https://doi.org/10.1017/S0016756817000334, 2018.

Reinecke, T.: Very-high-pressure metamorphism and uplift of coesite-bearing metasediments from the Zermatt-Saas zone, Western Alps, Eur. J. Mineral., 3, 7–18, https://doi.org/10.1127/ejm/3/1/0007, 1991.

Reynes, J., Jollands, M., Hermann, J., and Ireland, T.: Experimental constraints on hydrogen diffusion in garnet, Contrib. Mineral. Petrol., 173, 69, https://doi.org/10.1007/s00410-018-1492-z, 2018.

Reynes, J., Lanari, P., and Hermann, J.: A mapping approach for the investigation of Ti–OH relationships in metamorphic garnet, Contrib. Mineral. Petrol., 175, 46, https://doi.org/10.1007/s00410-020-01681-5, 2020.

Rossman, G. R. and Aines, R. D.: The hydrous components in garnets: Grossular-hydrogrossular, Am. Mineral., 76, 1153–1164, 1991.

Rossman, G. R., Beran, A., and Langer, K.: The hydrous component of pyrope from the Dora Maira Massif, Western Alps, Eur. J. Mineral., 1, 151–154, https://doi.org/10.1127/ejm/01/1/0151, 1989.

Rubatto, D., Gebauer, D., and Fanning, M.: Jurassic formation and Eocene subduction of the Zermatt–Saas-Fee ophiolites: implications for the geodynamic evolution of the Central and Western Alps, Contrib. Mineral. Petrol., 132, 269–287, https://doi.org/10.1007/s004100050421, 1998.

Rüpke, L. H., Morgan, J. P., Hort, M., and Connolly, J. A. D.: Serpentine and the subduction zone water cycle, Earth Planet. Sc. Lett., 223, 17–34, https://doi.org/10.1016/j.epsl.2004.04.018, 2004.

Schmädicke, E. and Gose, J.: Water transport by subduction: Clues from garnet of Erzgebirge UHP eclogite, Am. Mineral., 102, 975–986, https://doi.org/10.2138/am-2017-5920, 2017.

Schmädicke, E. and Gose, J.: Water in garnet of garnetite (metarodingite) and eclogite from the Erzgebirge and the Lepontine Alps, J. Metamorph. Geol., 38, 905–933, https://doi.org/10.1111/jmg.12554, 2020.

Schmidt, M. W. and Poli, S.: Experimentally based water budgets for dehydrating slabs and consequences for arc magma generation, Earth Planet. Sc. Lett., 163, 361–379, https://doi.org/10.1016/S0012-821X(98)00142-3, 1998.

Schwandt, C. S., Cygan, R. T., and Westrich, H. R.: Mg self-diffusion in pyrope garnet, Am. Mineral., 80, 483–490, https://doi.org/10.2138/am-1995-5-609, 1995.

Sheng, Y.-M., Xia, Q.-K., Dallai, L., Yang, X.-Z., and Hao, Y.-T.: H_2O contents and D / H ratios of nominally anhydrous minerals from ultrahigh-pressure eclogites of the Dabie orogen, eastern China, Geochim. Cosmochim. Ac., 71, 2079–2103, https://doi.org/10.1016/j.gca.2007.01.018, 2007.

Vho, A., Lanari, P., Rubatto, D., and Hermann, J.: Tracing fluid transfers in subduction zones: an integrated thermodynamic and

$\delta^{18}O$ fractionation modelling approach, Solid Earth, 11, 307–328, https://doi.org/10.5194/se-11-307-2020, 2020.

Xia, Q.-K., Sheng, Y.-M., Yang, X.-Z., and Yu, H.-M.: Heterogeneity of water in garnets from UHP eclogites, eastern Dabieshan, China, Chem. Geol., 224, 237–246, https://doi.org/10.1016/j.chemgeo.2005.08.003, 2005.